Evidence for preservation of organic carbon interacting with iron in material displaced from retrogressive thaw slumps: Case study in Peel Plateau, western Canadian Arctic

Journal Article

Author(s):
Thomas, Maxime; Monhonval, Arthur; Hirst, Catherine; Bröder, Lisa; Zolkos, Scott; Vonk, Jorien E.; Tank, Suzanne E.; Keskitalo, Kirsi H.; Shakil, Sarah; Kokelj, Steven V.; van der Sluijs, Jurjen; Opfergelt, Sophie

Publication date:
2023-05

Permanent link:
https://doi.org/10.3929/ethz-b-000608066

Originally published in:
Geoderma 433, https://doi.org/10.1016/j.geoderma.2023.116443

Geoderma 433 (2023) 116443

Contents lists available at ScienceDirect

Geoderma

journal homepage: www.elsevier.com/locate/geoderma

Evidence for preservation of organic carbon interacting with iron in material displaced from retrogressive thaw slumps: Case study in Peel Plateau, western Canadian Arctic

Maxime Thomas [a,*], Arthur Monhonval [a], Catherine Hirst [a], Lisa Bröder [b,c], Scott Zolkos [d,e,f], Jorien E. Vonk [b], Suzanne E. Tank [d], Kirsi H. Keskitalo [b], Sarah Shakil [d], Steven V. Kokelj [g], Jurjen van der Sluijs [h], Sophie Opfergelt [a]

[a] Earth and Life Institute, Université catholique de Louvain, Louvain-la-Neuve, Belgium
[b] Department of Earth Sciences, Vrije Universiteit Amsterdam, Amsterdam, the Netherlands
[c] Department of Earth Sciences, Swiss Federal Institute of Technology (ETH) Zürich, Switzerland
[d] Department of Biological Sciences, University of Alberta, Edmonton, AB, Canada
[e] John A. Paulson School of Engineering and Applied Sciences, Harvard University, MA, USA
[f] Woodwell Climate Research Center, Falmouth, MA, USA
[g] Northwest Territories Geological Survey, Yellowknife, NT, Canada
[h] Northwest Territories Centre for Geomatics, Yellowknife, NT, Canada

ARTICLE INFO

Handling Editor: Alberto Agnelli

Keywords:
Mineral-organic carbon interactions
Retrogressive thaw slumps
Mass wasting
Peel Plateau
Iron

ABSTRACT

In northern high latitudes, rapid warming is set to amplify carbon-climate feedbacks by enhancing permafrost thaw and biogeochemical transformation of large amounts of soil organic carbon. However, between 30 % and 80 % of permafrost soil organic carbon is considered to be stabilized by geochemical interactions with the soil mineral pool and thus less susceptible to be emitted as greenhouse gases. Quantification of the nature of and controls on mineral-organic carbon interactions is needed to better constrain permafrost-carbon-climate feedbacks, particularly in ice-rich environments resulting in rapid thaw and development of thermokarst landforms. On sloping terrain, mass wasting features called retrogressive thaw slumps are amongst the most dynamic forms of thermokarst. These multi-decadal disturbances grow due to ablation of an ice-rich headwall, and their enlargement due to warming of the Arctic is mobilizing vast stores of previously frozen materials. Here, we investigate headwall profiles of seven retrogressive thaw slumps and sediments displaced from these mass wasting features from the Peel Plateau, western Canadian Arctic. The disturbances varied in their headwall height (2 to 25 m) and affected land surface area (<1 to > 30 ha). We present total and water extractable mineral element concentrations, mineralogy, and mineral-organic carbon interactions in the headwall layers (active layer, permafrost materials above an early Holocene thaw unconformity, and Pleistocene-aged permafrost tills) and in displaced material (suspended sediments in runoff and material accumulated on the debris tongue). Our data show that the main mechanism of organic carbon stabilization through mineral-organic carbon interactions within the headwall is the complexation with metals (mainly iron), which stabilizes 30 ± 15 % of the total organic carbon pool with higher concentrations in near-surface layers compared to deep permafrost. In the displaced material, this proportion drops to 18 ± 5 %. In addition, we estimate that up to 12 ± 5 % of the total organic carbon is stabilized by associations to poorly crystalline iron oxides, with no significant difference between near-surface layers, deep permafrost and displaced material. Our findings suggest that the organic carbon interacting with the sediment mineral pool in slump headwalls is preserved in the material mobilized by slumping and displaced as debris. Overall, up to 32 ± 6 % of the total organic carbon displaced by retrogressive thaw slumps is stabilized by organo-mineral interactions in this region. This indicates that organo-mineral interactions play a significant role in the preservation of organic carbon in the material displaced from retrogressive thaw slumps over years to decades after their development resulting in decadal to centennial scale sequestration of this retrogressive thaw slump-mobilized organic carbon interacting with the soil mineral pool.

* Corresponding author.
E-mail address: maxime.thomas@uclouvain.be (M. Thomas).

https://doi.org/10.1016/j.geoderma.2023.116443
Received 11 June 2022; Received in revised form 16 February 2023; Accepted 18 March 2023
Available online 6 April 2023

1. Introduction

High-latitude regions are warming three times faster than the global average (AMAP, 2021). During 2007–2016, permafrost temperatures in the Arctic increased by up to 0.39 ± 0.15 °C (Meredith et al., 2019). Arctic permafrost environments have sequestered large amounts of organic carbon (OC) over thousands of years (Zimov et al., 2006), which are vulnerable due to climate-driven thaw (Dobricic and Pozzoli, 2019; IPCC, 2019). The northern permafrost region soils OC reservoir is estimated at 1460 to 1600 Pg of carbon (PgC) (i.e., twice as much as the carbon currently stored in the atmospheric pool) considering the top 0–3 m soil layer (Hugelius et al., 2014) and the deep carbon (Strauss et al., 2017). Models consistently predict that permafrost OC is vulnerable to thaw (Abbott and Jones, 2015; Koven et al., 2011; Lawrence et al., 2015; McGuire et al., 2018; Schuur et al., 2015; Turetsky et al., 2020), which could produce a positive feedback on global climate change by enhancing microbial methane (CH_4) and carbon dioxide (CO_2) production and emissions from the permafrost environments into the atmosphere (Friedlingstein et al., 2006; Schuur et al., 2008).

Best estimates indicate that 5 % to 15 % of the terrestrial permafrost OC reservoir is vulnerable to thaw and emission to the atmosphere as greenhouse gases by the end of this century (Plaza et al., 2019; Schuur et al., 2015). The rate at which this feedback will take place is a critical question for climate prediction models. These estimates of future permafrost OC emissions are based on simulated volumes of OC exposed by the increase in thaw depth, i.e., gradual thaw (Dobricic and Pozzoli, 2019). Yet, variation in permafrost carbon emissions will depend significantly on organic matter interactions with the soil mineral pool, which can stabilize OC and reduce its susceptibility to microbial degradation. Between ~ 30 % (in Arctic soils in general; Mueller et al., 2015) and ~ 80 % (in ice-rich permafrost called Yedoma deposits; Dutta et al., 2006) of the soil OC can be mineral-associated. Iron is a dominant metal involved in mineral-OC interactions in soils and sediments (Kaiser and Guggenberger, 2007; Kögel-Knabner et al., 2008; Lalonde et al., 2012; Mu et al., 2016, 2020). These interactions can be: (i) organo-mineral associations (Kleber et al., 2015) resulting from the interaction of OC with mineral surfaces (such as OC sorbed onto clay minerals or Fe-oxides, using cation bridges such as Ca or Mg); (ii) organo-metallic complexes resulting from the complexation of OC with metal ions (i.e., OC complexed with e.g. Al, Fe, Ca); and (iii) OC physical protection within soil aggregates which renders OC inaccessible for microorganisms (i.e., occluded, involving clay minerals, Fe-Al (hydr)oxides or carbonates in aggregates) (Lützow et al., 2006). Studies relating carbon turnover time to mineral–OC interactions range from decades to millennia (Kleber et al., 2015 and references therein).

Gradual increase in active layer thickness is not the only mode of permafrost degradation. Permafrost thaw in ice-rich (e.g., up to 50 % excess ice) environments can result in the rapid development of thermokarst landforms (Heginbottom et al., 2012; Kokelj and Jorgenson, 2013). Landscape consequences of ice-rich permafrost thaw are sometimes referred to as pulse disturbances named abrupt thaw, even though thermokarst processes can operate over timescales that vary by several orders of magnitude. On upland hillslope ice-rich terrains, these thermokarst landforms manifest as mass wasting features, namely retrogressive thaw slumps (RTS), gullies or active layer detachments (Kokelj and Jorgenson, 2013). During the 21st century under SSP5–8.5 (the Shared Socio-economic Pathway (SSP) corresponding to very high greenhouse gas emissions scenario; Fox-Kemper et al., 2021), the area susceptible to be affected by upland hillslope thermokarst landforms is estimated to increase by ~ 250,000 km^2 (to be compared with an increase of 1.6 million km^2 in total area susceptible to development of thermokarst landforms) and yet is predicted to account for one third of thermokarst carbon losses (Turetsky et al., 2020).

Retrogressive thaw slumps are amongst the most dynamic form of slope thermokarst. These thaw-driven mass wasting features are most abundant in ice-rich permafrost preserved glaciated terrain (Kokelj et al., 2017a). The disturbances enlarge due to ablation of an ice-rich headwall which produces meltwaters and a saturated slurry that accumulates in a scar zone. Depending on the ice-content of permafrost, material properties, slope and climate conditions, the materials may be translocated downslope by a range of geomorphic processes that include slopewash, creep, fluidized flows and deep seated plug-like flow. Recent climate driven acceleration of downslope sediment transport (Kokelj et al., 2015b, 2021) has produced large debris deposits in stream valleys where they are transiently stored until being gradually eroded. Debris tongues can extend from a few dozen to hundreds of meters long depending on the morphology of the slump (Kokelj et al., 2015a) and reach tens of meters in thickness (Kokelj et al., 2021, 2015a). The deposits may remain stable for decades to centuries (Kokelj et al., 2021; Murton and Ballantyne, 2017) with potential for debris to be refrozen after burial throughout much of their depth (Kokelj et al., 2009).

Slumps expose and relocate large volumes of previously frozen materials where increases in disturbance area are non-linearly related to the volume of materials displaced (Kokelj et al., 2021; van der Sluijs et al., 2022), involving masses of previously perennially frozen carbon which can potentially be biolabile (Bröder et al., 2022; Vonk et al., 2013). Knoblauch et al. (2021) show, e.g., that thaw slump induced exposition of ice-rich Pleistocene Yedoma deposits liberates organic matter which is rapidly decomposed into CO_2 and accounts for 0.8 % of thawed OC mineralized to CO_2 in one year. However, the processes driving (de)stabilization of OC by mineral interactions following retrogressive thaw slump development has received little attention. Previous studies note that thaw-slump induced microbial CO_2 production from displaced material can be stimulated by oxic conditions (Schädel et al., 2016). Changing redox conditions are also likely to affect the interactions between OC and redox-sensitive elements such as iron (Herndon et al., 2020; Monhonval et al., 2021b, 2022; Patzner et al., 2020). Recent studies show, however, that OC displaced by thaw slumps is mainly mobilized in particulate form and that this particulate OC undergoes minimal oxidation over an aerobic incubation period while being potentially protected by OC-mineral interactions (e.g., Shakil et al., 2020, 2022). Nevertheless, the mineral-OC interactions could potentially evolve between the initial headwall-origin (i.e., permafrost and active layer source) material and the sediments mobilized by slumping forming the debris. This could have unknown, yet critical implications for the release or sequestration of the mobilized OC. It follows that a better quantification of the forms and proportions of mineral-associated OC in slumps and their debris tongues is required (Opfergelt, 2020). In addition, the evolution of these interactions following thaw slump development is needed to better constrain the contribution of those mass wasting features to the permafrost carbon feedback.

Here, we hypothesize that thaw slump development displaces and mixes shallow and deep permafrost materials along with surface organic materials and modern vegetation and modifies (increases or decreases) the proportions of mineral associated OC in downslope deposits (i.e., the material mobilized from thaw slumps after permafrost thaw) relative to the headwall-origin materials (i.e., prior to slump initiation). Shallow and deep permafrost material are potentially contrasting both in terms of their mineral associated OC content and their relative mass proportion in the displaced material. We test this hypothesis across a series of thaw slumps of varying thicknesses of exposed permafrost (i.e., concavity depths), to understand how variation in mixing of shallow and deep material, affects mineral associations in displaced materials. We therefore characterize the permafrost materials from a series of contrasting headwall exposures and materials displaced from those thaw features for their proportion of mineral associated OC.

2. Materials and methods

2.1. Study area

The Peel Plateau straddles the continuous and extensive discontinuous permafrost zones (as defined in Obu et al., 2018) in the Northwest Territories of Canada. This physiographic region spans 24,000 km^2 across the eastern periphery of both the Richardson and Mackenzie Mountains (Kokelj et al., 2017b). The sampling sites are located in the 1,100 km^2 Stony Creek watershed which drains into the Peel River. It is located west of the town Fort McPherson (Fig. 1 A-C), situated approximately 115 km southwest of the town of Inuvik. The Peel Plateau is a fluvially incised landscape underlain by thick (up to 100 m), ice-rich (~50 % by volume; Lacelle et al., 2013) Pleistocene-aged glacial deposits. Surficial geology is comprised of tills, glaciofluvial, lacustrine and colluvial deposits (Duk-Rodkin and Hughes, 1992). Materials span a range of grain size, but the fine-grained tills distributed through the region are prone to slides and flows when saturated. These sediments contain carbonates, sulfides, sulfates and silicates (Zolkos et al., 2018).

From 18,700 to ~ 13,500 cal. yr. BP, the region was covered by the Laurentide Ice Sheet (LIS; Dalton et al., 2020). Subsequent warming in the early Holocene (ca 9,000 cal. yr. BP) caused an increase in thaw depths and associated development of RTS features (Lacelle et al., 2019). Across the western Canadian Arctic coast region, an increase in active layer thickness (the relict active layer was 2.5 fold thicker than that of todays' ~50 cm) (Burn, 1997), and thaw-driven colluviation enabled mineral weathering, leaching of solutes and incorporation of organic matter in the upper few meters of soil (Burn, 1997; Malone et al., 2013; Lacelle et al., 2019). Many exposures reveal evidence of talik development (residual "peat islands"; Van der Sluijs et al., 2018) and past thaw slumping. The latter resulted in integration of slumped surface material into the colluvial soils which can be detected by a higher solute content than exposures which have undergone leaching (Lacelle et al., 2019). These contrasting profiles of Holocene-modified deposits have been preserved in a layer situated immediately below the present-day active layer and above the ice-rich Pleistocene-aged tills. The parent materials across stratigraphic units are therefore of common origin. The transition between the unmodified perennially frozen Pleistocene-aged permafrost and the permafrost deposits modified during the Holocene is marked by a thaw unconformity (Lacelle et al., 2013, 2019). The Holocene and the deeper Pleistocene permafrost layers are distinguished stratigraphically by this thaw unconformity typically encountered 1.5 – 3 m below the surface (Malone et al., 2013). Today, the region is characterized by a subarctic, continental climate. The mean annual air temperature in 2017 was 4.8 °C at Inuvik (daily average) and 3.6 °C in Fort McPherson (hourly average, Environment Canada, 2021). Vegetation is characterized by tundra at higher elevations in the west and by spruce forests in valleys at lower elevations in the east (O'Neill et al., 2015). Fluvial incision of the Peel Plateau and an abundance of ground ice favor the development of thaw slumps (Kokelj et al., 2017a) which is accelerating with recent warming and increasing rainfall (Kokelj et al., 2015b; Lacelle et al., 2010; Lantuit et al., 2012).

2.2. Site selection and sampling locations

Seven thaw slumps sites with contrasting size and morphology were selected within the Stony Creek watershed (slumps FM2, FM3, SE, SD-CB, SF, HC, HD, Table 1; Fig. 1). Samples were collected in two separate sampling campaigns (A and B) during the summer of 2017 (mid-July to mid-August) in five different sampling locations at each slump. Three sampling locations are located at the slump headwall (Fig. 2 A): (i) the active layer (~50 cm thick; denoted AL); (ii) the Holocene-modified deposits containing previously thawed sediments (denoted HO) and (iii) the Pleistocene-aged permafrost deposit (denoted PL). Two sampling locations are located in the downstream debris composed of displaced material sampled from a few hundred meters to one kilometer from the thaw slump headwall (Fig. 2 A): (i) suspended sediments undergoing active transport in runoff considered as a yearly deposit (denoted RU) and (ii) sediments from the debris tongue accumulated for decades (denoted DT). In campaign A, we sampled the headwall layers of slumps FM2, FM3, CB and SF. These samples are AL samples (n = 9), HO samples (n = 5) and PL sample (n = 1). These samples have been analyzed for organic matter content, radiocarbon age and biomarker concentrations in Bröder et al. (2021). In sampling campaign B (n = 35), slumps FM2, FM3, SD (immediately downstream from CB sampled during campaign A), SE, SF, HC and HD were sampled once at all sampling locations (i.e., AL, HO, PL, RU and DT). Samples from sampling campaign B have been analyzed to characterize the inorganic carbon cycling in Zolkos and Tank (2020).

2.3. Bulk element concentrations

We assessed the total concentrations of calcium (Ca), potassium (K), iron (Fe), aluminum (Al) and silicon (Si) in all samples except HD-RU (n = 49) using a portable X-ray fluorescence (XRF) device (*Niton XL3t GOLDD* + pXRF; ThermoFisher Scientific, Waltham, the United States). The measurements were performed in laboratory (ex-situ) conditions on air-dried samples to avoid introduction of additional variability (e.g., water content, sample heterogeneity). Briefly, samples were placed on a circular plastic cap (2.5 cm diameter), its base covered with a thin transparent film (prolene 4 μm). Minimum sample thickness in the cap was set to 2 cm to prevent underestimation of the detected intensities (Ravansari et al., 2020) and total time of analysis is set to 90 s to standardize each measurement. The pXRF-measured concentrations were calibrated for trueness using a method following Monhonval et al. (2021a). In the following, the total element concentration measured by XRF and corrected for trueness will be referred to as Ca_t, K_t, Si_t, Fe_t. A complete description of the sites used and the calibration method can be found in the supplementary information.

The total organic carbon (TOC) content on all samples except HD-RU and FM3-AL (sampling campaign A) (n = 48) was measured using a Thermo Fisher Elemental Analyser (FLASH 2000 CHNS/O) at the National Research Council, Institute of Polar Sciences in Bologna (Italy).

2.4. Mineralogical analysis

The X-ray diffraction (XRD) method allows the characterization of the presence of crystalline mineral phases. We assessed the mineralogy of 25 finely ground bulk samples from sampling campaign B (slumps FM2, FM3, SE, SD, SF). Mineralogy was already available for slumps HC and HD from Zolkos and Tank (2020). The mineralogy of the bulk samples was determined on non-oriented powder finely ground in a mortar (Cu Kα, Bruker Advance D8 diffractometer, detection limit 5 % by weight).

2.5. Selective mineral elements extractions

Four procedures of selective extraction from soil were used as indicators of the water-extractable, complexed, poorly crystalline oxides, and crystalline oxide phases (Rennert, 2019). More specifically: (i) the water extraction (2 g in 20 mL of ultrapure water, i.e., resistivity range = 10–18 MΩ·cm) for 2 h at room temperature targets elements released in soluble phase (Ca, K, Fe, Si, S). When the measured concentrations of water extracted Fe were below the quantification limit, a value of 2/3 of the quantification limit was used (Reimann et al., 2008); (ii) the sodium pyrophosphate extraction of Fe, Al and Mn targets the organo-metallic complexes (Bascomb, 1968; Parfitt and Childs, 1988). A contribution of oxide nanoparticles in addition to the organically-bound metals is possible (Jeanroy and Guillet, 1981), but limited by centrifugation and filtration of the extract; (iii) the dark ammonium oxalate extraction of Fe targets poorly crystalline oxides (i.e., poorly crystalline oxides and organo-metallic complexes, Blakemore et al., 1981); iv) the dithionite-

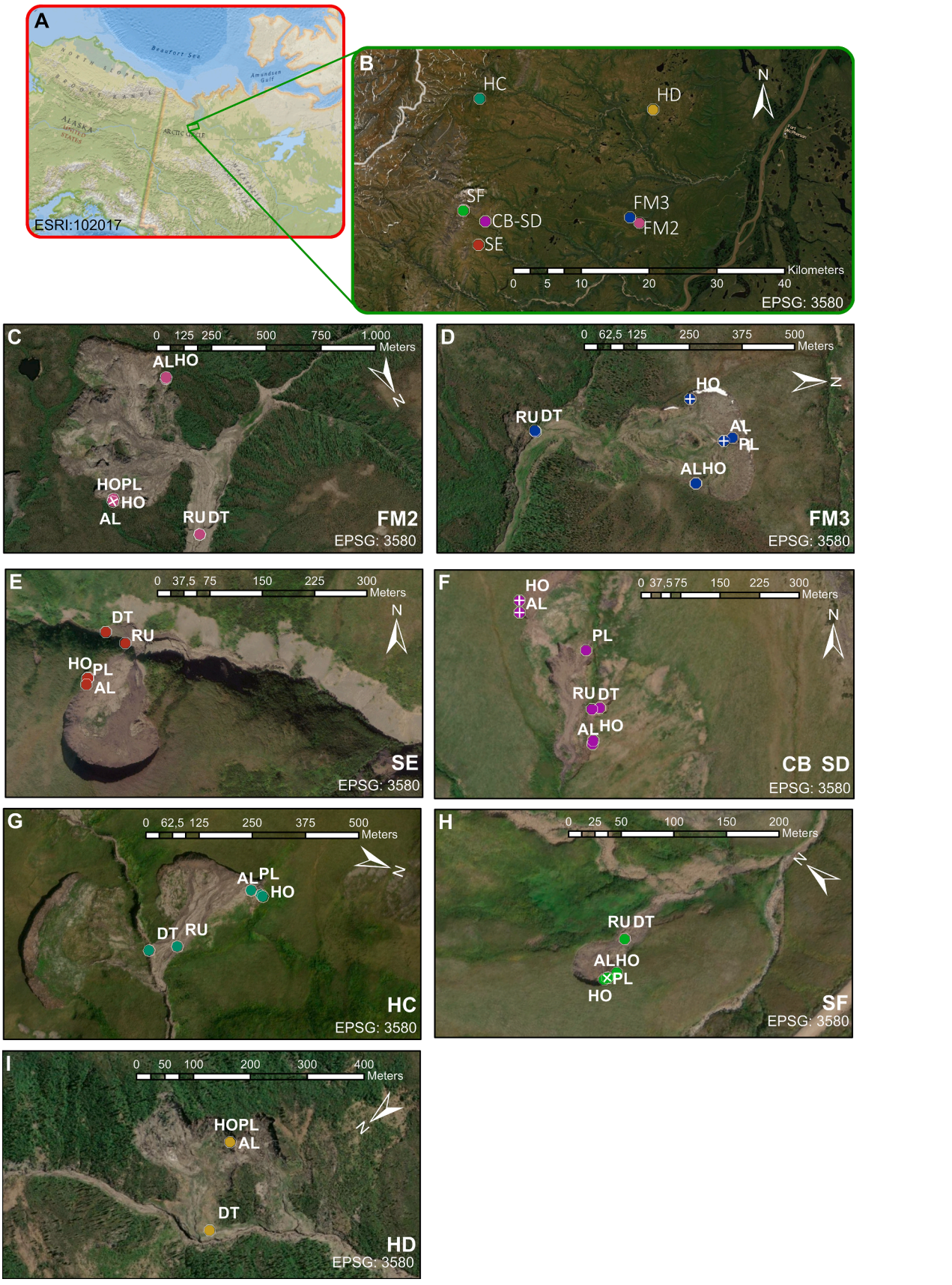

(caption on next page)

Fig. 1. Retrogressive thaw slump extent and morphology within the Peel Plateau. (A-B) Sampling sites. (C-I) Sampling locations (summer 2017) at each slump. Colors in panel B corresponds to the colors in panels C-I to identify the corresponding slump. Sampling locations from sampling campaign A are presented by a cross in colored circles and sampling locations from sampling campaign B are represented by empty colored circles. Three sampling locations are located at the slump headwall: (i) the active layer (denoted AL); (ii) the Holocene-modified deposits (denoted HO) and (iii) the Pleistocene-aged permafrost deposit (denoted PL). Two sampling locations are located in the downstream debris composed of displaced material: (i) suspended sediments undergoing active transport in runoff (denoted RU) and (ii) sediments from the debris tongue (denoted DT). Projected coordinate systems are presented by ESRI or EPSG code. Map created in ArcMap 10.8. Basemap layer credits: World Ocean Base: Esri, GEBCO, NOAA, National Geographic, Garmin, HERE, Geonames.org, and other contributors, National Geographic World Map: National Geographic, Esri, Garmin, HERE, UNEP-WCMC, USGS, NASA, ESA, METI. World Imagery: Esri, Maxar, GeoEye, Earthstar Geographics, CNES/Airbus DS, USDA, USGS, AeroGRID, IGN, and the GIS User Community. World boundaries and places: Esri, HERE, Garmin, (c) OpenStreetMap contributors, and the GIS user community, Esri, Garmin, GEBCO, NOAA NGDC, and other contributors.

Table 1
Retrogressive thaw slumps characteristics and morphology. Characteristics are derived from published values and field estimations. Metrics correspond to thaw slumps as they were at the time of sampling, i.e., 2017. ND = no data.

Slump	Scar zone area (ha) *	Headwall height (m) **	Year of initiation ***	AL depth (cm)		Growth rate (m y^{-1}) ****
				Sampling campaign A	Sampling campaign B	
FM2	32.7 [a]	18.6	1944	40	23	15
FM3	6.7 [a]	6.5	1958	50	65	12.5
SD	< 1 [b]	2.7	~ 2013	ND	46	ND
CB	2.5 [c]	5.8	2002–2004	60	ND	ND
SE	1.5 [c]	17.9	~ 2013	ND	27	ND
SF	0.4 [c]	5.6	ND	40	56	ND
HC ¤	2.5 [d]	13.3	ND	ND	39	ND
HD	0.6 [d]	8.5	ND	ND	44	ND

¤ Site **HC** is comprised of five separate slump features that have merged into two scar zones (Littlefair et al., 2017).
* excludes area of debris tongue [a] Van der Sluijs et al. (2018); [b] from field observations (Zolkos et al., 2018); [c] ArcMap estimate; [d] Zolkos and Tank (2020).
** Zolkos and Tank (2019), average; CB from Kokelj et al. (2021); FM2: mean from FM2-morph 5 in suppl info from Zolkos and Tank (2019).
*** RTS year of occurrence. **FM2** | 1993 (Zolkos et al., 2018); 1944 (Malone et al., 2013); 1954 (Brooker et al., 2014). **FM3** | 1958 (Malone et al., 2013). **CB** | from Kokelj et al. (2021). **SD**, **SE** | estimated from field observations and remote sensing imagery.
**** **FM2** from Brooker et al. (2014) via Zolkos et al. (2018), **FM3** in Lacelle et al. (2015a) via Littlefair et al. (2017).

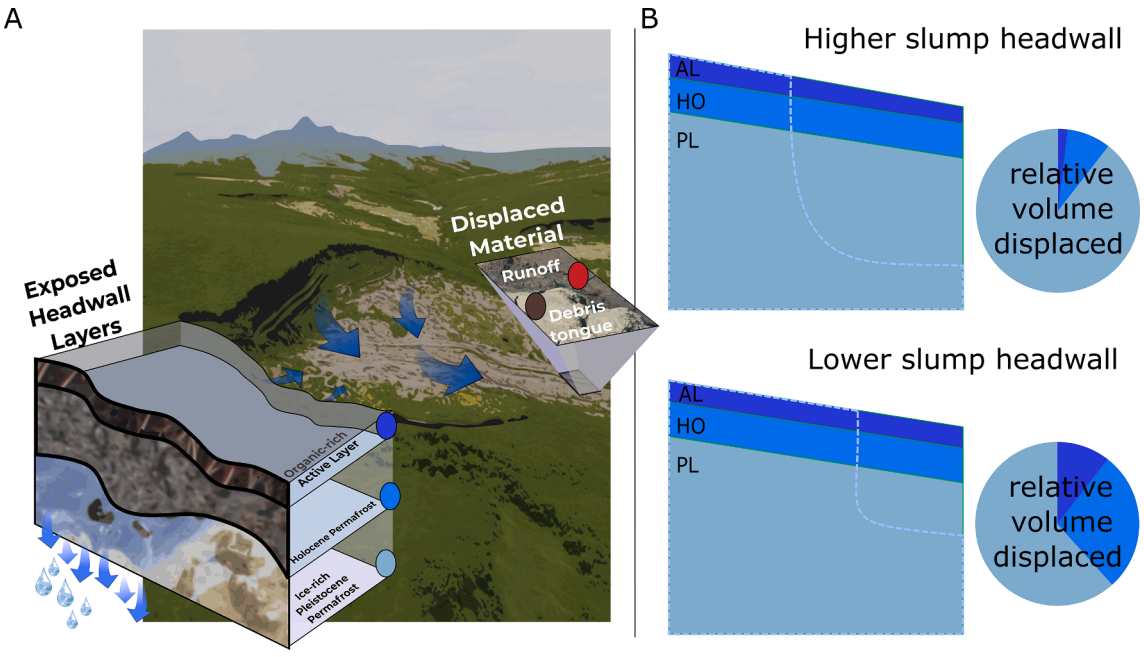

Fig. 2. (A) **Conceptual model and sampling locations on a thaw slump headwall and displaced material and** (B) **contrasted original headwall layer contributions to the displaced material**. Three categories of samples were collected from the slump headwall (i) the active layer (<1 m thick; denoted AL; dark blue); (ii) the Holocene-modified deposits containing previously thawed sediments (denoted HO; medium blue) and (iii) the Pleistocene-aged permafrost deposit (denoted PL; light blue). Two categories of samples were collected from the downstream debris composed of displaced material: (i) suspended sediments undergoing active transport in runoff (denoted RU; red) and (ii) sediments from the debris tongue (denoted DT; brown). The higher the concavity depth of a thaw slump, the greater the relative proportion of deeper ice-rich till within the debris tongue.

citrate-bicarbonate extraction (DCB) extraction of Fe targets free Fe oxides, i.e., poorly crystalline and crystalline oxides (McKeague and Day, 1966; Mehra and Jackson, 1958).

The water extraction was carried out on the whole set of samples (n = 50) and the pyrophosphate, oxalate and DCB extractions were carried out on slumps FM2, FM3, SD, SE, SF and HC from sampling campaign B (n = 30) due to limited amount of sample. Element concentrations were measured in solution by ICP-OES after each selective extraction. In the

following, the elements extracted by water, pyrophosphate, oxalate and DCB methods will be referred to as the corresponding element symbol followed by a subscripted letter indicating the type of extraction, namely 'w' for water extraction (Ca_w, K_w, Fe_w, Si_w, S_w), 'p' for pyrophosphate extraction (Fe_p, Al_p, Mn_p), 'o' for oxalate extraction Fe_o), and 'd' for DCB extraction (Fe_d).

2.6. Selective organic carbon extractions

The pool of OC selectively extracted with sodium pyrophosphate (Bascomb, 1968; Jeanroy and Guillet, 1981; Parfitt and Childs, 1988) and dark ammonium oxalate (Blakemore et al., 1981) was measured on the same solutions as those used for the selective extractions of metals (n = 30; section 2.5). Briefly, (i) for carbon involved in organo-metallic complexes, we measured dissolved OC released after dispersion by pyrophosphate using a Shimadzu TOC-L® analyzer (measuring non-purgeable OC). In the following, this carbon extracted by pyrophosphate will be referred to as C_p; (ii) for oxalate extracted carbon, we evaluated the organic acid concentration in the oxalate extract by measuring the absorbance at 430 nm via a Genesys 10 S VIS spectrophotometer, with the extractant solution as a blank. The optical density of the oxalate extract (ODOE) is mainly influenced by the extracted fulvic acids thereby indicating the concentration in organic acids present in the oxalate extract (Daly, 1982).

2.7. Modeling approach for calculating the contributions of the headwall layers to downstream material composition

To model the chemical composition of material exported from the headwall and mixed in the scar zone area, we selected two slumps of contrasting headwall heights (FM2: 18.6 m on average; FM3: 6.5 m; Zolkos and Tank (2020) and Table 1) and contrasting volumes exported (FM2: $60 \cdot 10^5$ m^3, Kokelj et al., (2021) and van der Sluijs et al. (2018); FM3: $50 \cdot 10^4$ m^3, Kokelj et al. (2021) and van der Sluijs et al. (2018)). We used volume estimates to derive the relative mass of each characteristic layer of the headwalls (i.e., AL, HO and PL) that have been displaced since the initiation of the slump.

For the volume estimates, we used thaw slump scar zone cut volume estimates provided by Van der Sluijs et al. (2018). Briefly, the total volume of material displaced by thaw slumps FM2 & FM3 was derived by differencing a 2017 remotely piloted aircraft system (RPAS)-derived digital surface model (DSMs) from pre-disturbance terrain surface (Van der Sluijs et al., 2018). Pre-disturbance terrain surface (accuracy considered to be 1 m) was manually reconstructed using airborne laser scanning-derived 2-m contours aided by historical aerial photographs and circa 1970 Canadian Digital Elevation Data (CDED) digital elevation model (DEM). Digital surface models of the slumps FM2 and FM3 were obtained from highly overlapping RPAS photos processing in Pix4D (Van der Sluijs et al., 2018).

We considered only the scar zone cut volume within the scar zone area as it was in 2017 (see blue delineation - Van der Sluijs et al., 2018 - Fig. 3 for FM2). Within each cell volume (1 m resolution) in the scar zone, the relative proportion of each characteristic layer of the sampling location was calculated as follows: (i) assessing the active layer is 0.5 m thick (Table 1; Zolkos and Tank, 2020), the first 0.5 m (maximum) of height contributes to AL; (ii) assessing Holocene deposits are approximately 2-meter-thick (Burn, 1997; Lacelle et al., 2015b), the next 2 m of height (maximum) were attributed to HO and (iii) the remaining height

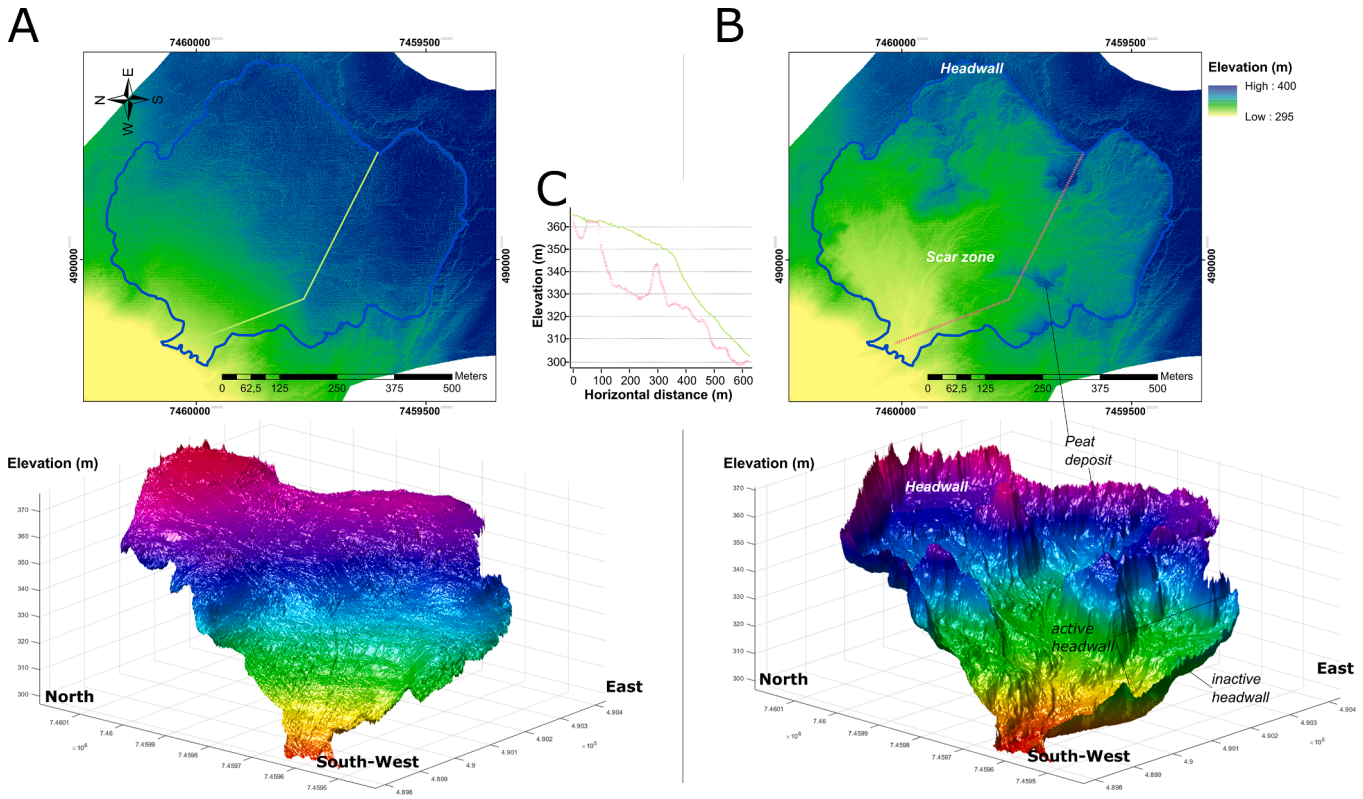

Fig. 3. Modeling approach for calculating thaw slump scar zone cut volume. The total volume of material displaced by thaw slumps FM2 and FM3 was derived by differencing a 2017 remotely piloted aircraft system (RPAS)-derived digital terrain model (DTMs) from pre-disturbance terrain surface (Van der Sluijs et al., 2018). (A) Pre-disturbance terrain surface was manually reconstructed using airborne laser scanning-derived 2-m contours aided by historical aerial photographs and circa 1970 Canadian Digital Elevation Data (CDED) digital elevation model (DEM); (B) RPAS-derived 2017 DTMs served as input for slump after disturbance. Blue line shows the scar zone of the thaw slump feature; (C) Elevations transects of reconstructed pre-disturbance terrain surface (green line) and slump after disturbance (dashed red line). Transect lines are presented in insets A (green) and B (red). This figure presents slump FM2. A field photo from a similar perspective as inset B is presented in Figure S2. 1. Maps created in ArcMap 10.8 with projected coordinate system EPSG:3155. 3-D models created in MatLab R2018a.

was attributed to PL. The total volume of each layer is the sum of all corresponding cell sub-volumes.

For the mass calculations, we assumed (i) a volumetric mass density of 1 g·cm^{-3} (Iwahana et al., 2005; Strauss et al., 2017) and no ice content within AL; (ii) a 20 % volumetric ice content and a solid phase density of 2.65 (Shakil et al., 2020) within HO and (iii) a 50 % volumetric ice content (Lacelle et al., 2013) and a solid phase density of 2.65 (Shakil et al., 2020) within PL. By knowing the total mass of each headwall stratigraphic layer (AL, HO and PL), we calculated the mass proportion of each layer. The modeled concentration (e.g., total iron, in mg_{Fe} per kg soil) of the material exported was therefore calculated by multiplying the measured concentration in each headwall sample (AL, HO and PL) by the mass proportion of the corresponding layer and sum all contributions.

2.8. Statistical analysis

We performed computations for statistical analysis using R software version R.3.6.1 (R Core Team, 2019). Compact displays of data distributions were performed using violin plots (mirrored density plots) combined with boxplots showing five summary statistics: the median, two hinges for the 25th and 75th percentiles and two whiskers that extend from the hinges to 1.5 times the inter-quartile range. Outliers beyond the whiskers are plotted individually (Hintze and Nelson, 1998; McGill et al., 1978). Robust linear regression (R^2 adj) presented in this study are implemented with an alpha of 0.95. When numerical statistics are presented in the text for dataset descriptions, the mean ± standard deviation of the distribution is presented. For comparing two datasets, we performed nonparametric statistical Wilcoxon test. P-values for these tests are available in the Table S3. 1.

3. Results and discussion

3.1. Thaw history dictates the concentrations of total and soluble elements and mineral-bound organic carbon within retrogressive thaw slump headwall layers

Similar to past studies, our data show contrasting mineral element concentrations within the different layers exposed in retrogressive thaw slump headwalls (Lacelle et al., 2019; Malone et al., 2013; Zolkos and Tank, 2020). The deeper permafrost layers (PL) are characterized by significantly higher (p- value < 0.05) total concentrations in Ca (7 ± 2 g/kg) and K (22 ± 5 g/kg) than concentrations observed within the active layer (4 ± 3 g/kg for Ca_t and 18 ± 3 g/kg for K_t; Fig. 4 A, B). The shallower permafrost layers (HO) present concentrations in Ca_t (7 ± 3 g/kg) and K_t (20 ± 1 g/kg) that are intermediate between the active layer (AL) and the deep permafrost (PL) (Fig. 4 A, B). These observations are in line with evidence of contrasting profiles within the Holocene-modified deposits following different types of past permafrost degradation (Lacelle et al., 2019). For less soluble major elements such as Fe and Si, the total concentrations (41 ± 7 g/kg for Fe_t and 316 ± 37 g/kg for Si_t) do not differ between layers in the headwall (Fig. 4 C, D), despite a wider range of Fe_t and Si_t concentrations in the active layer than in the permafrost layers (HO and PL). The TOC concentrations are significantly different between the active layer (40 ± 39 g/kg) and the permafrost layers (18 ± 7 g/kg; p-value < 0.05; Table S3. 1), with consistently higher values in the active layer (Fig. 4 E).

The proportion of highly soluble water extractable elements such as

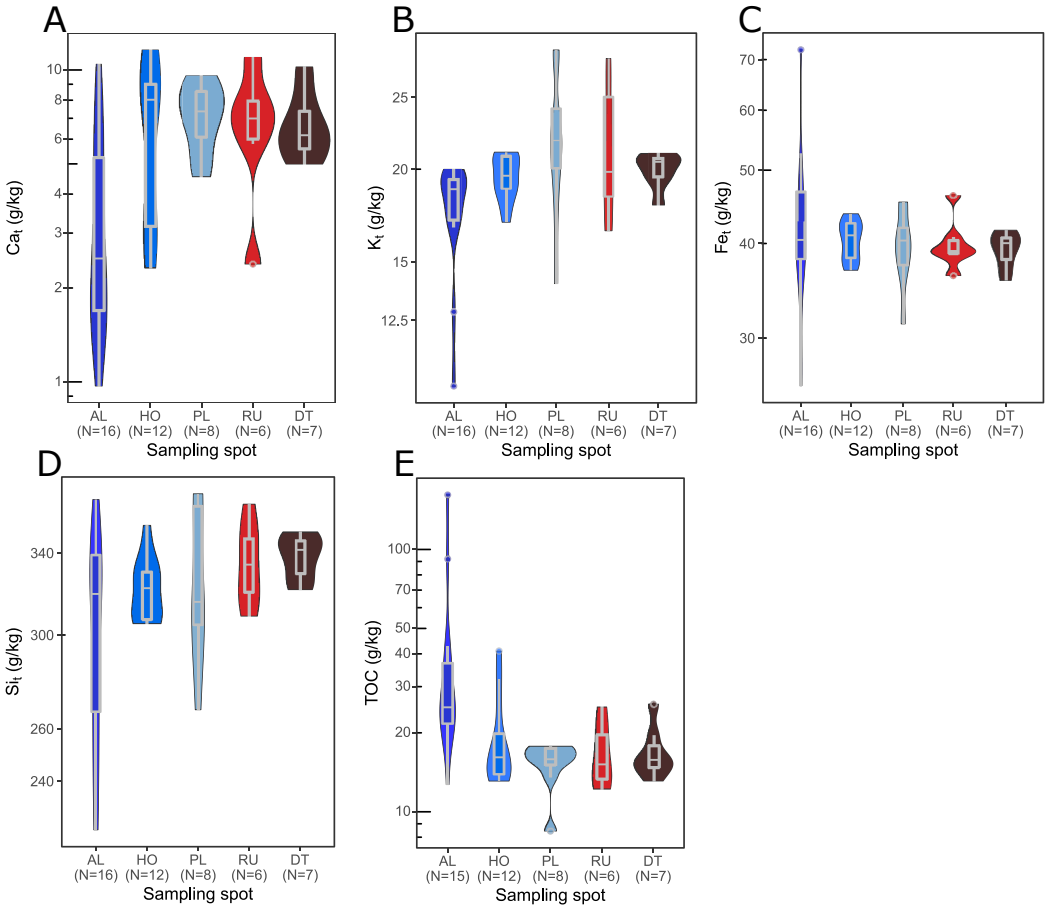

Fig. 4. Violin plots of the Ca_t (A), K_t (B), Fe_t (C), Si_t (D) and total organic carbon (E) concentrations within the active layer (AL), Holocene permafrost (HO) and Pleistocene permafrost (PL) compared to suspended sediments (RU) and debris (DT) on all samples (n = 49) from the 7 thaw slumps studied. Color code as in Fig. 2.

Ca and K is one order of magnitude greater in deep permafrost layers (PL; 12 ± 10 % for Ca_w/Ca_t and 3 ± 1 ‰ for K_w/K_t) than in the active layer (AL; 1 ± 1 % for Ca_w/Ca_t and 1 ± 0.9 ‰ for K_w/K_t; Fig. 5 A, B). These observations are consistent with the high proportions of soluble elements reported in the deep permafrost layer (PL; Lacelle et al., 2019; Malone et al., 2013; Zolkos and Tank, 2020). For less soluble elements such as Si and Fe, the proportion of water extractable elements is higher in the active layer than in permafrost layers (Fig. 5 C, D), despite the similar total concentrations in these elements (Fig. 4 C, D). The proportion of water extractable Ca and K in the shallower permafrost layer dated from the Holocene (HO; 7 ± 13 % for Ca_w/Ca_t and 3 ± 2 ‰ for K_w/K_t) are intermediate between the concentrations in the seasonally thawed active layer (AL) and in ice-rich tills at depth, which have remained frozen since their emplacement. This likely reflects variability within the paleo-thaw unconformity (Lacelle et al., 2013, 2019) between different slumps and suggests that some Holocene-modified deposits samples (HO) have thawed in the past, while other HO layer samples may have thawed only briefly, or been part of a colluvial deposit. In some cases, colluviated substrate from former thaw slump scar areas was incorporated into permafrost during its subsequent aggradation (Lacelle et al., 2019). In addition, gypsum is detected in the HO layer of the FM3 slump - a HO layer presenting a higher water extractable Ca concentration (Figure S4. 2) - which shows that indeed locally, mineral weathering has been limited. The past thaw history of present-day exposed headwall material would therefore be the prevalent controller of soluble mineral element concentrations in sediments (Lacelle et al., 2019).

Interactions between Fe and OC, as Fe-OC complexes and as OC-Fe oxide associations, were investigated in six slumps (FM2, FM3, SD, SE, SF and HC) from sampling campaign B in the different headwall layers. The proportion of Fe bound to OC in the form of complexes relative to total Fe (Fe_p/Fe_t) is one order of magnitude higher in the active layer than in the ice-rich tills at depth (PL; p-value < 0.05). This represents a proportion of 8 ± 3 % of the total Fe that is in complexed form in the active layer versus 0.6 ± 0.3 % for the ice-rich tills at depth (PL). The Holocene-modified deposits show greater variability with 6 ± 6 % of total Fe in complexed form (Fig. 6 A). Within the active layer, OC forming complexes (C_p) with metals (i.e., Fe, Al, Mn) represents 37 ± 3 % of the TOC, while this proportion is 35 ± 18 % in the HO layer and decreases to 17 ± 11 % for the deep permafrost layer (PL). Overall (i.e., considering all analyses of headwall samples with identical importance), OC-metal complexes stabilize 30 ± 15 % of the TOC pool, with a higher proportion of OC stabilized in near-surface layers compared to deep permafrost. Our data therefore show that not only is the deep permafrost layer less concentrated in TOC than the AL and HO layers, but the proportion of OC bound to metals is also significantly lower in this layer (Table S3. 1). However, literature data showed that both HO-aged layers that experienced increasing thaw depth and undisturbed permafrost (PL) contain mainly old low-degradable organics suggesting that further degradation is unlikely to occur now (Bröder et al., 2021; Shakil et al., 2022).

The proportion of complexed Fe and poorly crystalline Fe-oxides (Fe_o/Fe_t, i.e., the ratio between the oxalate-extracted Fe concentration and the total Fe concentration; Fig. 6 D) does not differ between the

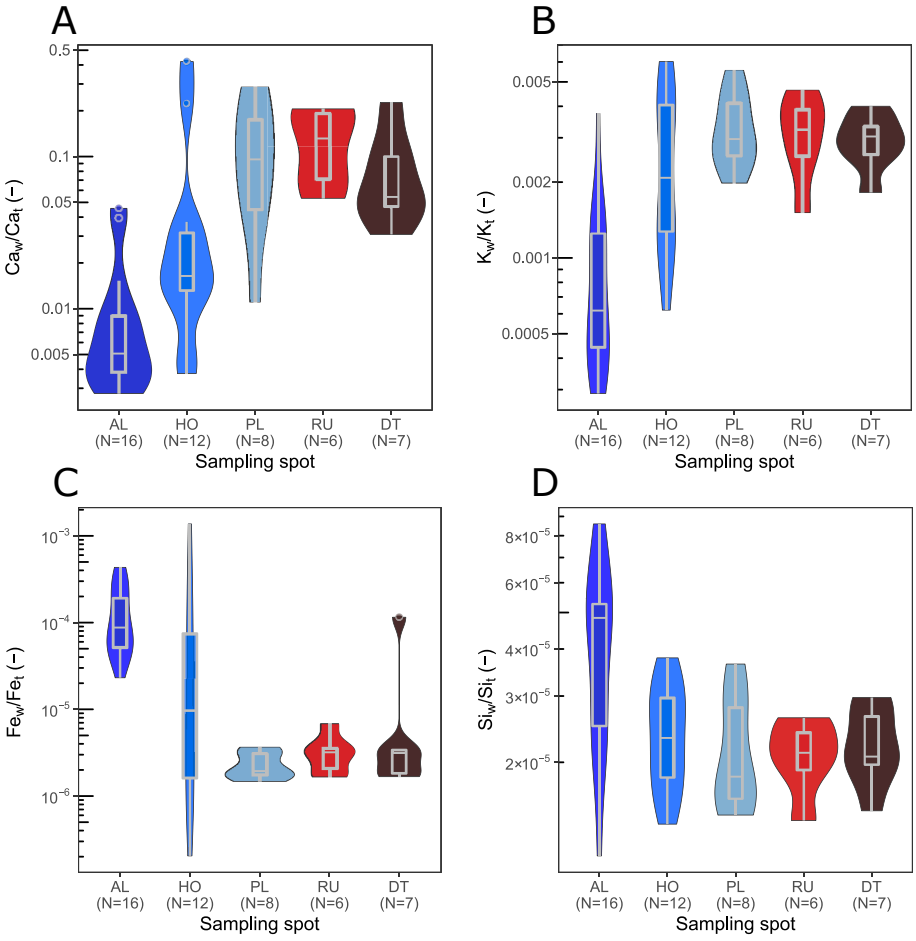

Fig. 5. Violin plots of the ratio between water extracted (w) and total (t) concentrations for Ca (A), K (B), Fe (C), Si (D) within the active layer (AL), Holocene permafrost (HO) and Pleistocene permafrost (PL) compared to displaced suspended sediments (RU) and debris (DT) on all samples (n = 49) from the 7 thaw slumps studied. Color code as in Fig. 2.

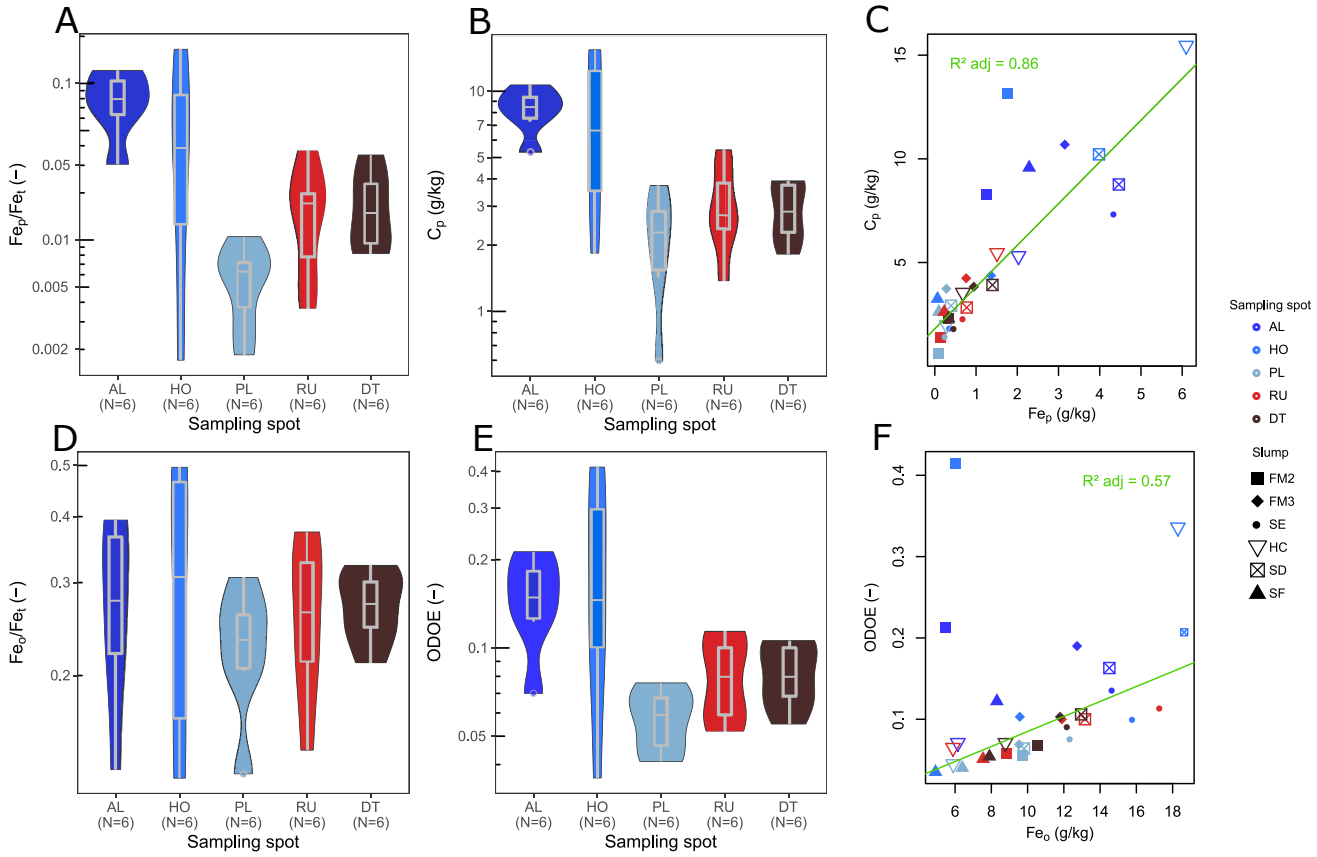

Fig. 6. Violin plots of the ratio Fe_p/Fe_t (A), C_p (B) and a robust linear regression plot between C_p and Fe_p (C); Violin plots of the ratio Fe_o/Fe_t (D), optical density of oxalate extract (ODOE) (E) and a robust linear regression plot between ODOE and Fe_o (F) for slumps FM2, FM3, SD, SE, SF and HC from sampling campaign B. Active layer = AL, Holocene permafrost = HO, Pleistocene permafrost = PL, suspended sediments = RU and debris = DT. Color code as in Fig. 2. Note the log scale on the violin plots.

stratigraphic layers, with an average proportion of 28 ± 12 %. An evaluation of the organic acid concentration in the oxalate extract is provided by its optical density (ODOE). The ODOE decreases significantly between the active layer and the deep permafrost layer (p- value < 0.05; Fig. 6 E; Table S3. 1). The ODOE correlates with the concentration in Fe_o (R^2adj = 0.57; Fig. 6 F), but shows an even higher correlation with the concentration in C_p (R^2adj = 0.78). The variance of the ODOE is mainly explained by the concentration in OC forming complexes with metals. This supports that the organic acids present in the oxalate extracts are dominated by OC from metal complexes relative to OC adsorbed onto poorly crystalline Fe oxides.

The proportion of poorly crystalline Fe-oxides ((Fe_o - Fe_p)/Fe_t) is 23 ± 9 % on average for headwall material for all slumps. Assuming a maximum sorption capacity of 0.22 g_{OC}/g_{Fe} as ferrihydrite (Wagai and Mayer, 2007), we can estimate a maximum proportion of 11 ± 5 % of TOC bound to poorly crystalline Fe oxides (Fe_o–Fe_p) within the headwall layers. This means that the proportion of OC bound to poorly crystallized Fe oxides (OC-Fe oxide associations relative to the TOC) is no more than half the proportion of OC forming complexes (C_p/TOC, 30 ± 15 %) in headwall layers, even though the concentration of complexed Fe is only 5 ± 5 % of total Fe in headwall layers on average (i.e., only a small percentage of the total Fe content in a slump is required to complex 34–40 % of the TOC in the active layer). Iron concentrations in sediments from the Peel Plateau are comparable to concentrations in Yedoma deposits (exact site locations in section S1; Monhonval et al., 2021b), with a distribution of Fe within the same range for Fe as organic complexes (7 ± 6 % in Yedoma deposits, Monhonval et al., 2021b; 5 ± 5 % in Peel headwall samples) and in poorly crystallized Fe oxides (12 ± 7 % in Yedoma deposits, Monhonval et al., 2021b; 23 ± 9 % in Peel headwall samples). In both Peel Plateau and Yedoma regions, stabilization of OC through interactions with the mineral pool appears to be dominated by complexation with metals (35 ± 25 % in Yedoma deposits, Monhonval et al., 2021b; 30 ± 15 % in Peel headwall samples) rather than through associations with poorly crystallized Fe oxides (6 ± 6 % in Yedoma deposits, Monhonval et al., 2021b; 11 ± 5 % in Peel headwall samples). Moreover, it can be argued that within the headwall, sediments that have experienced thaw (i.e., modern-day or paleo active layers) contain proportions of OC interacting with the mineral pool that are significantly higher than in the ice-rich tills at depth. Past thaw history is therefore a main control on the mineral-associated OC concentrations in permafrost soil and sediments.

3.2. *Thaw slump development transfers solute-rich and highly weatherable deep sediments downslope*

In the material transferred downslope from the seven thaw slumps, the Ca_t and K_t concentrations reflect prevalent contribution from the deepest permafrost layer (PL; Fig. 4 A, B). Indeed, the debris tongues (DT; 7 ± 2 g/kg for Ca_t and 20 ± 1 g/kg for K_t) are characterized by a significantly higher concentration of Ca_t and K_t (p-value < 0.05; Table S3. 1) than in the active layer (AL; 4 ± 3 g/kg for Ca_t and 18 ± 3 g/kg for K_t), but show a similar concentration to the deep permafrost layer (PL). The Fe_t and Si_t concentrations in the displaced material are similar to all three headwall layers (Fig. 4 C, D), whereas the TOC in the displaced material (DT; 17 ± 4 g/kg) presents lower concentrations relative to active layer (AL; 40 ± 39 g/kg) and similar concentrations relative to the deep permafrost layer (PL; 15 ± 4 g/kg; Fig. 4 E; p- value < 0.05). The proportion of water extractable elements for Ca, K, Si and

Fe is similar in permafrost at greater depth (PL) and in displaced material (RU and DT; Fig. 5 A, B, C, D). Overall, we never observed a significant difference in total and water extractable concentrations between the deep permafrost deposits (PL) and the material transferred downslope. Thaw slump development thus exposes and displaces ice- and solute-rich highly weatherable deep sediments frozen since the Pleistocene (Malone et al., 2013; Zolkos and Tank, 2020). Our data confirm that some sediment characteristics (i.e., total and water extractable Ca, K, Fe, Si concentrations) are preserved from weathering in displaced suspended sediments and debris for days (RU) to decades (DT) (see also Zolkos and Tank, 2020).

The Ca_w and S_w concentrations are overall higher in suspended sediments (RU) compared to debris accumulated for about ten years or more (DT) (Fig. 5 A): Ca_w concentration is on average 1.6 times higher in the suspended sediments (RU, 1,020 ± 630 $mg{\cdot}kg^{-1}$) than in the debris (DT, 710 ± 530 $mg{\cdot}kg^{-1}$) and S_w concentration is on average 1.8 times higher in the suspended sediments than in the debris (1,300 ± 740 $mg{\cdot}kg^{-1}$ in RU and 740 ± 650 $mg{\cdot}kg^{-1}$ in DT). Mineralogical data show that soluble mineral phases (e.g., gypsum) from the deep permafrost (PL) are transferred downstream and preserved in the suspended sediment (RU; shown for the three slumps FM2, SE, SF, Figure S4. 1, Figure S4. 3, Figure S4. 5), and not detected in the accumulated deposits (DT). There is however reported evidence of gypsum in the debris (DT) from slumps FM2, HC and HD (Zolkos and Tank, 2020), and higher solute concentrations in Ca, K, Mg, Na, Sr in the deep permafrost layers (PL) and the displaced material (RU and DT) than in the active layer, associated with a higher conductivity (Kokelj and Burn, 2005; Malone et al., 2013; Zolkos and Tank, 2020, 2019). The debris tongue sediments, although they appear to be depleted in soluble elements (e.g., Ca, S) to some extent, still show high concentrations in these elements, i.e., orders of magnitude higher than in the active layer.

3.3. Suspended sediments and debris deposits downslope integrate mineral-bound organic carbon contributions from each thaw slump headwall layer

The proportion of complexed-Fe is significantly higher (on average more than two-fold greater) in the downstream debris (DT) compared to the deep permafrost layer (p-value < 0.05; Fig. 6 A; Table S3. 1). Suspended sediments (RU) and debris (DT) show a proportion of complexed Fe relative to the total Fe (i.e., Fe_p/Fe_t) of 2 ± 1 % compared to 0.6 ± 0.3 % for deep permafrost (PL). This suggests that there is a significant contribution of complexed Fe from the active layer and Holocene deposits to the displaced sediments. In these sediments, the proportion of OC forming complexes with metals (C_p) represents on average 18 ± 5 % of the TOC (Fig. 6 B), and there is a strong correlation between the concentration in Fe_p and C_p ($R^2adj = 0.86$; Fig. 6 C). Among the metals involved in these complexes, Fe dominates (52 ± 16 %, on a molar basis) followed by Al (40 ± 13 %) and Mn (8 ± 7 %; Table S5. 1, Figure S5. 2). Similar to the concentration of Fe_p, the concentration of C_p is significantly higher in the active layer relative to the deep permafrost (p-value < 0.05; Table S3. 1), but contrary to Fe_p, we observe no significant difference in C_p concentration between the deep permafrost (PL) and the downslope exported material (RU, DT; p-value > 0.3; Fig. 6 B; Table S3. 1). Aluminum and manganese concentrations, also involved in OC complexation (i.e., Al_p and Mn_p), show less contrasted concentrations between the active layer and the deep permafrost layer (Figure S5. 2 B, C) and the sum of the metal complexes ($Fe_p + Al_p + Mn_p$) show no significant difference between the suspended sediments in runoff, debris and deep permafrost layer (p-value > 0.17; Figure S5. 2 D). These different distributions in metal complexes (Fe_p, Al_p, Mn_p) may possibly explain the fact that C_p is not significantly different between the ice-rich tills at depth (PL) and the displaced material (RU and DT).

We estimate a maximum proportion of 14 ± 4 % of TOC bound to poorly crystalline Fe oxides (Fe_o-Fe_p) across sites in the suspended sediments (RU) and debris originating from thaw slump headwalls (for all sampling locations taken together, i.e. AL, HO, PL, RU and DT, this proportion is 12 ± 5 %). This means that the maximum proportion of OC bound to poorly crystallized Fe oxides (OC-Fe oxide associations relative to the total) is not significantly different than the proportion of OC forming complexes (C_p/TOC) in the suspended sediments and debris. Overall, up to 32 ± 6 % of the TOC displaced by retrogressive thaw slumps is stabilized by organo-mineral interactions. Our data suggest that the contribution of the active layer to C_p concentrations in the suspended sediments and debris is significant but diluted compared to the contribution of the PL layer. In other words, the contribution of the active layer in displaced materials is only visible when concentrations of the particular element are much higher than in ice-rich tills at depth, i.e. orders of magnitude higher, as is the case for Fe_p. Suspended sediments and debris downslope therefore appear to be dominated by the prevalent contribution of ice-rich tills.

The results from these selective Fe and carbon extractions suggest that the concentration of OC associated with Fe of the displaced material (suspended sediments in runoff or in the debris tongue) reflects the mixing of the Pleistocene-aged permafrost at depth (i.e., poor in Fe-OC complexes) and the active layer and Holocene-modified deposits (i.e., enriched in Fe-OC complexes). These significant differences are observed within the six slumps studied for selective carbon and metal extractions, despite the slumps being distributed over a relatively large area (1600 km^2, Fig. 1) and representing a large size continuum (thaw slump headwall heights range from 2 to 25 m, Table 1).

3.4. Thaw slump displaced material composition can be quantitatively predicted using contributions from the headwall-origin layers

We hypothesize that the greater the contribution of the deep permafrost layer compared to the active layer, the more prominently the resulting geochemical properties of the exported material will bear characteristics of the deep permafrost layer. In other words, within thaw slumps with contrasting headwall heights, the exported materials can be expected to possess characteristics proportional to the relative contributions of the original headwall layers. This mixing hypothesis is also formulated in Littlefair et al. (2017) for dissolved organic carbon (DOC), Shakil et al. (2020) for particulate OC (POC) and e.g. Zolkos and Tank (2020) for solutes. The conceptual model for this assumption is presented in Fig. 2B.

We observe that as the ratio between the thickness of the active layer (considering that active layer is approximately 0.5-meter-thick; Zolkos and Tank, 2020) over the total headwall height (ratio AL height/total headwall height) increases, the concentration of Fe complexed with OC increases (positive linear relationship) in the exported material (RU, DT, Fig. 7 A, $R^2adj = 0.27$). The same increasing trend is observed for pyrophosphate carbon (C_p, Fig. 7 B, $R^2adj = 0.20$). This reflects the higher concentration of Fe_p and C_p in the active layer and HO permafrost than in the deeper PL tills (Fig. 6; section 3.3). We observe decreasing Ca_w and Ca_t concentration in the debris when the ratio AL depth/total headwall height increases (negative linear relationship, Fig. 7 C, D, $R^2adj = 0.16$ for Ca_w, $R^2adj = 0.58$ for Ca_t). This reflects the higher concentration in Ca_w and Ca_t in deep permafrost than in other headwall layers (Fig. 4 A, Fig. 5 A; section 3.1). For less soluble major elements such as Fe and Si, the total concentrations (Fe_t and Si_t) do not differ between layers in the headwall and we see no difference in the resulting concentrations within the exported material (Fig. 7 E, F, $R^2adj < 0$). Additional studies would be required to determine if such linear relationships represent a regional signature or if they are applicable to other regions where thaw slumps are abundant (e.g., Lewkowicz and Way, 2019; van der Sluijs et al., 2022; Young et al., 2022).

The ratio AL depth/total headwall height is not the only parameter influencing the variance of this dataset. There is some variability in the concentrations measured between the different thaw slumps (represented by the whiskers of the boxplots in Figs. 4-6). Shakil et al. (2020) acknowledge that landscape position likely plays an important role as e.

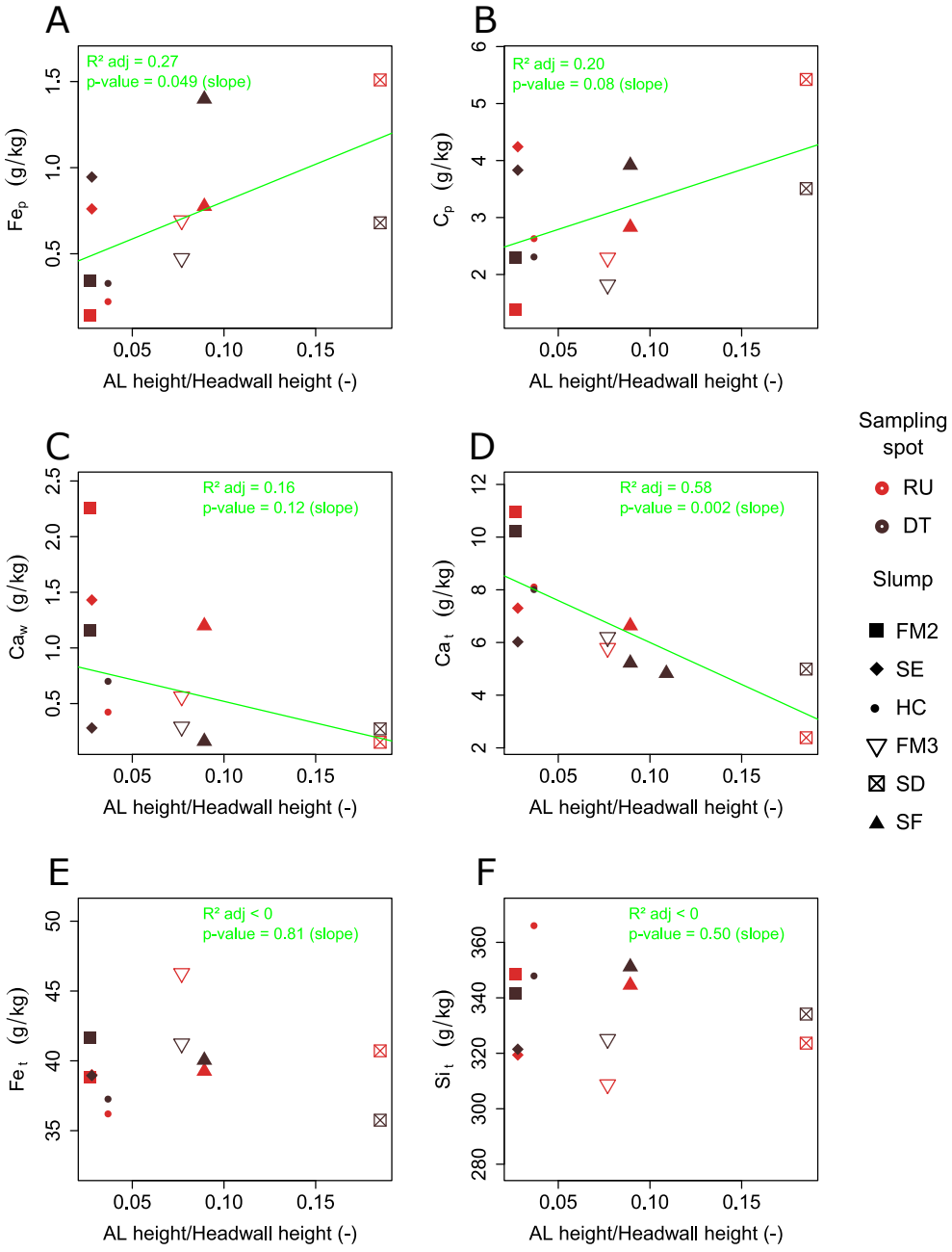

Fig. 7. Robust linear regression between the ratio of the active layer (AL) depth over the headwall height (based on data from sampling campaign B; Table 1) as a function of the Fe_p (A), C_p (B), Ca_w (C), Ca_t (D), Si_t (E) and Fe_t (F). p = pyrophosphate extract, w = water extract, t = total. suspended sediments = RU, debris = DT. The AL depth was estimated to be 0.5 m. Color code as in Fig. 2.

g., TOC yields increase to a greater degree westwards on the Peel Plateau, with closer proximity to maximum extent of the Laurentide ice-sheet limits (greater elevation, relative relief and abundance of glacio-fluvial/glaciolacustrine deposits and sparser tundra vegetation). Moreover, the contribution of the active layer thickness to the headwall height is not uniform within a slump. The sampling locations along the headwall (sampling campaign A and B; Table 1) can contribute to the variance of the dataset, as does variation in the relative contribution of the HO-modified deposits to the displaced material. To improve the understanding of the system, it would be worth further exploring variation (in thickness and composition) in the relict ground ice deposits and in the HO layer, both within and between sites.

Further, Kokelj et al. (2021) explored power law relationships between thaw slump area and volume, and between slump area and thickness of permafrost thawed (i.e., concavity depth). These simple models for active, cuspate-shaped slumps enable estimates of the volume and thicknesses of permafrost thawed, and the latter dictating the relative contributions of headwall-origin layers concentrations to composition of the material displaced from thaw slumps. Van der Sluijs et al. (2022) further explores area-volume models for slumps of varying activity levels across a wide range of geomorphic settings, while improving tools to estimate slump volumes and associated uncertainties. These approaches and related models can extend the findings of this work to regional or landscape levels by deriving depths of thaw within each scar zone and eroded volumes of a large sample of slumps.

3.5. Headwall-origin iron-organic carbon complexes are preserved in sediments mobilized by slumping and displaced as debris

Since new refreshed headwall material is exposed each summer, we hypothesize the modeled concentrations of the displaced material to be representative of its composition at the time of export. We compare these estimates to the measured concentrations after short-term (RU) and decadal evolution (DT). We test this hypothesis on the two mega-slumps (Table 1) of this study representing contrasted headwall heights, i.e., FM2 and FM3, by estimating the mass balance of the original headwall contributions, and then modeling the thaw slump downslope material composition.

Using the method presented in section 2.7, we estimated the contribution of each layer (AL, HO, PL) in mass to the total mass exported from the two mega-slumps FM2 and FM3. In slump FM2, the active layer represents a contribution of 2.0 % in mass in the material exported, whereas in slump FM3, active layer represents a contribution of 4.6 % in mass in the material exported (Table 2). We acknowledge that variations in thickness of the Holocene layer (HO; i.e., depth to relict ice) is highly variable across the landscape (within and between slumps). The relative contribution of the deep permafrost (PL) layer to the downstream displaced material is 24 % higher in mass in slump FM2 than in FM3 (Table 2). By contrast, shallow permafrost (HO) contribution to the displaced material is 21 % lower in mass in slump FM2 than in FM3.

The modeled concentrations in Ca_w, S_w, Si_w, C_p, Fe_p and TOC in the displaced material are of the same order of magnitude as the concentrations of these elements measured in the actual deposits (i.e., RU and DT; Fig. 8). More specifically, the modeled concentrations in Ca_w and S_w being lost from slump features seem closer to the concentrations of suspended sediments in runoff (RU) than to debris (DT) accumulated for decades. This is likely due to the fact the RU deposits represent recently displaced material, thus are more representative of the conditions of the exported material at the time of the collapse. We hypothesize that in older deposits (DT), a portion of the soluble elements such as Ca and S could have been leached following the dissolution of the more soluble phases (section 3.2). Zolkos and Tank (2020) however show high solute production associated with debris tongue sediments on slumps FM2, HC and HD, indicating that this weathering has been somewhat limited.

The similarity in concentrations in C_p and Fe_p in the modeled and in the sampled sediments, suggests that there is limited change in the concentration of organo-metallic complexes in sediments mobilized by slumping as suspended in runoff or accumulated in the debris (Fig. 8). This implies that slumping and material exposure is not accompanied by a change in the proportion of OC forming complexes between the original sediments from the headwall and the deposits. Our mixing hypothesis is therefore verified, and our results suggest that OC-mineral interactions are largely preserved in the displaced materials but that there was minimal formation of new organo-metallic complexes. It can be noticed that the differences between modeled and measured concentrations are opposite between the two slumps. More specifically, (i) the modeled Ca_w and S_w concentrations are lower than the measurement data at FM2 and higher at FM3; and (ii) the modeled Fe_p and C_p concentrations and TOC content are higher than the measurement data at FM2 and lower at FM3 (Fig. 8). We interpret this by an effect of the strong differences in the concentrations in the Holocene layer (HO) between the two slumps. We observe higher concentrations in Ca_w in slump FM3 (2 g/kg) compared to FM2 (0.2 g/kg). The same is true for S_w (2 g/kg for FM3 and 0.06 g/kg for FM2). For slump FM3, these high concentration values in the Holocene permafrost layer lead to high modeled concentrations of those water-extracted elements. For the pyrophosphate extraction, it is the opposite: C_p in the Holocene permafrost layer is lower for FM3 (0.4 g/kg) than FM2 (2 g/kg) and the same is true for Fe_p (2 g/kg for FM3 and 13 g/kg for FM2). For slump FM3, the low concentration values in the Holocene permafrost lead to low modeled concentrations of those pyrophosphate extracted elements. The TOC content follows the same pattern as pyrophosphate extractions. Yet it is reasonable to assume that what is found in the materials suspended in runoff (RU) and in the debris (DT) represents the integrated signature of the headwall composition as a whole and not the local effects of either very high or very low concentrations within the Holocene permafrost. Therefore, we recognize the importance of further acknowledging the variability found within the Holocene layer in and between slumps, and the limitation of assuming homogeneous element concentrations in the Holocene layer in our model.

Regarding the fraction of OC stabilized by associations with poorly crystalline Fe-oxides, our results highlight that there is no significant difference in the proportion of poorly crystalline Fe-oxides between headwall layers (AL, HO, PL; $(Fe_o\text{-}Fe_p)/Fe_t = 23 \pm 9$ %) and deposits (RU and DT; $(Fe_o\text{-}Fe_p)/Fe_t = 25 \pm 7$ %). This indicates that the sorption capacity of poorly crystalline Fe oxides to stabilize OC is maintained between the original sediments and the deposits. For the older deposits which have faced the longest post-deposition period (DT), we estimate that the proportion of organic carbon stabilized within the six slumps studied is up to 31 ± 5 % of the TOC. More precisely, 18 ± 5 % of the TOC is stabilized as complexes with metals, and maximum 13 ± 3 % of the TOC is bound to poorly crystalline Fe oxides by sorption. These data support that about one third of the TOC in the deposits is stabilized by interactions with Fe and other metals (Al, Mn) as complexes.

Table 2
Headwall-origin layer contributions by volume and mass displaced from slumps FM2 and FM3. AL = active layer; HO = Holocene-modified deposits; PL = Pleistocene-aged permafrost deposit.

	FM2			FM3		
	AL	HO	PL	AL	HO	PL
Volume (m^3)	$1.6 \cdot 10^5$	$6.5 \cdot 10^5$	$50.9 \cdot 10^5$	$3.3 \cdot 10^4$	$12.7 \cdot 10^4$	$31.1 \cdot 10^4$
Proportion of total volume	2.8 %	10.9 %	86.3 %	7.0 %	27.0 %	66.0 %
Total volume (m^3)		$60 \cdot 10^5$			$5 \cdot 10^5$	
Mass of solid phase (kg)	$1.6 \cdot 10^8$	$13.7 \cdot 10^8$	$67.4 \cdot 10^8$	$3.3 \cdot 10^7$	$27.0 \cdot 10^7$	$41.2 \cdot 10^7$
Proportion of total mass	2.0 %	16.5 %	81.5 %	4.6 %	37.7 %	57.7 %
Total mass (kg)		**$80 \cdot 10^8$**			**$7 \cdot 10^8$**	

3.6. Implications for the mass of organic carbon exported

Shakil et al. (2020) estimated that ~ $1.1 \cdot 10^8$ kg of slump-origin POC was mobilized in debris tongue deposits since the initiation of the slumps, as sum of slumps FM2 and FM3. This study confirms this assessment by estimating a mass of TOC exported of $1.3 \cdot 10^8$ kg for FM2 and $0.1 \cdot 10^8$ kg for FM3 (Fig. 9). The proportion of TOC that is stabilized (i.e., as complexes with metals or by associations with poorly crystalline Fe oxides) is 25 % and 31 % respectively for slumps FM2 and FM3. Overall, the relative contribution of stratigraphic layers to TOC in the displaced material varies between slumps FM2 and FM3 (Fig. 9), confirming that spatial variability from one thaw slump headwall to the other (section 3.4) will dictate the composition of the exported material.

Our study shows that metal–organic carbon interactions as complexes or involving poorly crystalline Fe oxide phases play a significant role in the preservation of stabilized organic carbon after thaw slump development and material displacement over years to centuries (Fig. 9) and to a distance (for RU and DT sampling locations) from a few hundred meters to a maximum of one kilometer from the headwall (AL, HO and PL) (Fig. 1). These observations are in line with past work suggesting that most of the permafrost OC released from slumps FM2 and FM3 is primarily in the form of particulate OC (Shakil et al., 2020) and has little potential to be mineralized within the stream system (Bröder et al., 2021; Keskitalo et al., 2021; Shakil et al., 2022). Nevertheless, it must be emphasized that remobilization of these deposits further in the debris

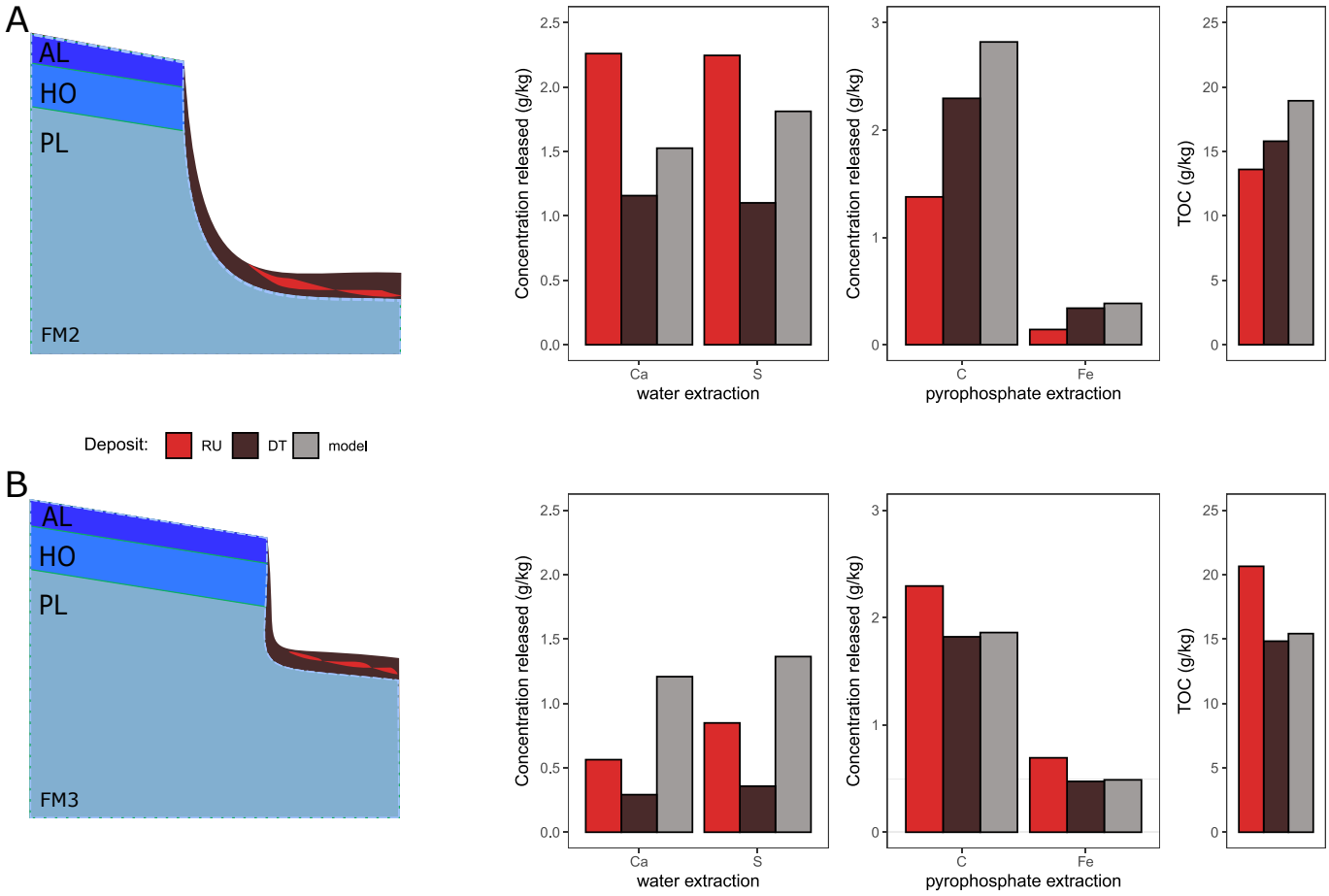

Fig. 8. Thaw slump displaced material composition modeling and comparison to in-situ measurements for slumps FM2 (A) and FM3 (B). Modeled concentrations (gray) have been generated from the concentrations in the different layers of the headwall weighted by their mass proportion and compared to actual displaced suspended sediments (RU) and the debris (DT). Color code as in Fig. 2.

tongue and the downstream cascade through stream networks (Kokelj et al., 2021) by fluvial processes could include changes in redox conditions. Following Kokelj et al. (2021), the sediment remobilization from FM2 represents a debris tongue volume of 2×10^6 m^3 (to be compared with a scar volume of 6×10^6 m^3), a portion of which extends to several kilometers downstream of the headwall. Changes in redox conditions with sediment mobilization to fluvial networks might lead to an evolution of the proportions of metals forming complexes with OC, but also with poorly crystalline and crystalline forms of Fe and to associations between Fe and the OC (Monhonval et al., 2021b). Although particulates dominate OC release from RTSs on the Peel Plateau by orders of magnitude (Shakil et al., 2020, 2022), thaw-released DOC by slumping is shown to be highly biolabile on the Peel Plateau (Littlefair and Tank, 2018) and similarly, studies on coastal thaw slumps have shown CO_2 emissions associated with these thermo-erosional features (Tanski et al., 2021, 2017). These carbon fluxes must therefore also be considered in order to obtain an exhaustive carbon balance for a system as complex as a thaw slump. This study therefore highlights the need of using a sedimentary cascade sampling scheme framework to have an accurate representation of organic carbon release and transformation from thaw slumps through the fluvial network over time.

The mass of TOC exposed by the mega-slump FM3 represents 8 % of the mass of TOC exposed by slump FM2 (Fig. 9). This implies that the exposure of deep Pleistocene-aged permafrost materials, even though less concentrated in organic carbon than the other layers, induces a mass of mobilized TOC that exceeds the mass of TOC mobilized by the active layer and the shallow permafrost. We acknowledge that is likely not true for shallow slumps with smaller headwall heights, but following the power-law relationships between thaw slump area and volume of material thawed (Kokelj et al., 2021; van der Sluijs et al., 2022), we note that the total mass of OC displaced by small, shallow slumps will similarly be orders of magnitude lower than the masses mobilized by a mega-slump like FM2. Available radiocarbon age data (Bröder et al., 2021) on similar samples show intermediate $\Delta^{14}C$ in the displaced suspended sediments and debris (RU and DT; $\Delta^{14}C = -841 \pm 118$ ‰) relative to ice-rich tills at depth (PL; $\Delta^{14}C$ = -976.2 ‰) and active layer (AL; $\Delta^{14}C$ = -563 ± 210 ‰), which confirm our findings that displaced materials reflect the mixing of the PL layer (relatively poor in metals-OC complexes) and the AL (relatively enriched in metal-OC complexes; Fig. 10 A). It should be mentioned, however, that since the contribution of Holocene-modified deposits is intermediate and variable in terms of mass contribution, it would be important to characterize this variability to obtain a more comprehensive model. This mixing is also supported by biomarker data on the OC ratios of even low molecular weight *n*-alkanes ($LMW_{16,18,20}$) to odd high molecular weight *n*-alkanes ($HMW_{27,29,31}$) showing the contribution from petrogenic or microbially altered organic matter from the deep permafrost layer (Bröder et al., 2021; Fig. 10 B). The evolution of the OC pool exposed by slumping not only depends on the OC composition, but also on the portion of OC stabilized by mineral interactions. Our data demonstrate that the mixing of different sources of OC results in about one third of the TOC being mineral-associated (32 ± 6 %; section 3.3). This includes mineral associations as metal complexes (18 ± 5 %) or bound to poorly crystalline Fe oxides (up to 14 ± 4 %) in the displaced material, with lower proportion of mineral-associated OC in petrogenic or microbially altered organic matter from ice-rich tills at depth (Fig. 10 B). This is in the low range of the

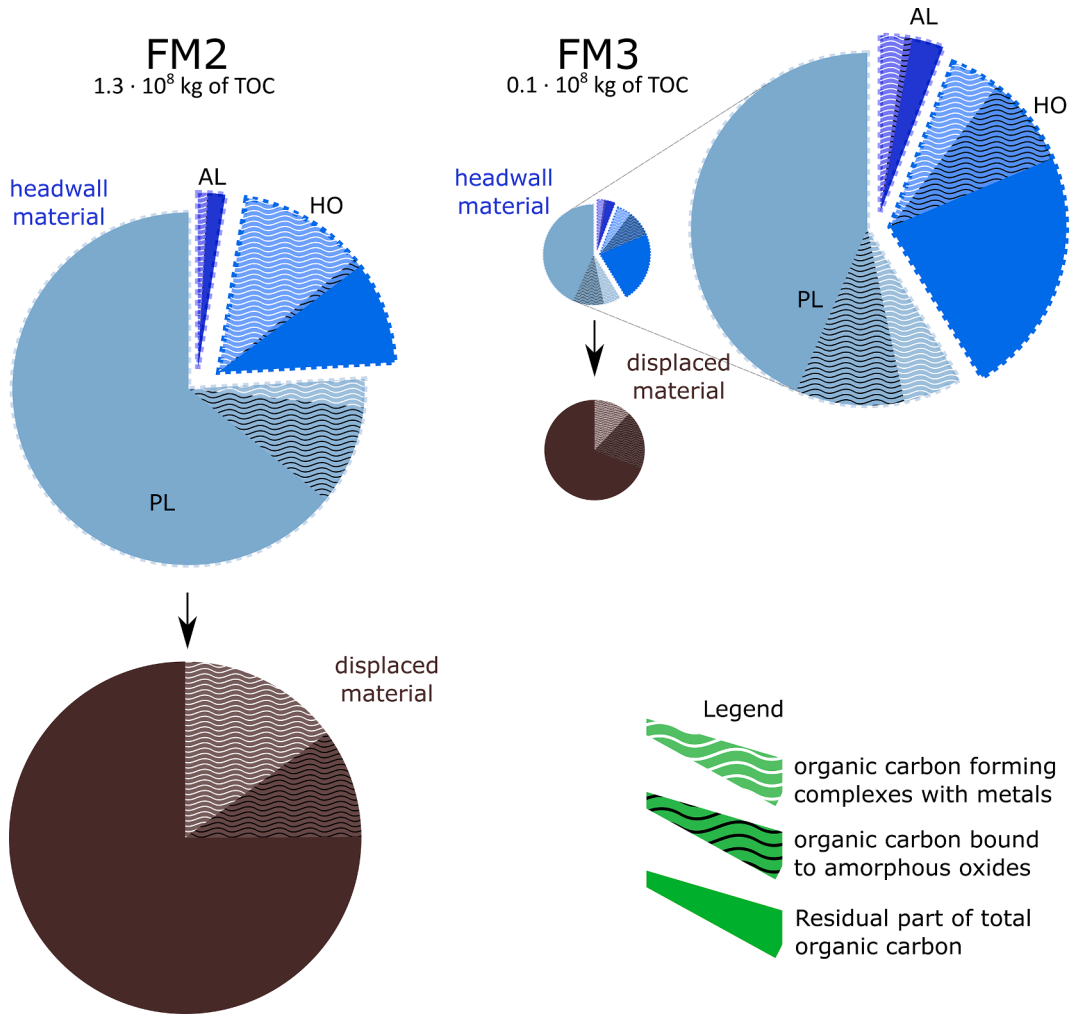

Fig. 9. Mass balance of organic carbon exported by the mega-slumps FM2 and FM3, with contrasted headwall heights and relative proportions of the different forms of organic carbon mobilized by slumping and displaced downslope. Active layer = AL, Holocene permafrost = HO, Pleistocene permafrost = PL. Color code as in Fig. 2.

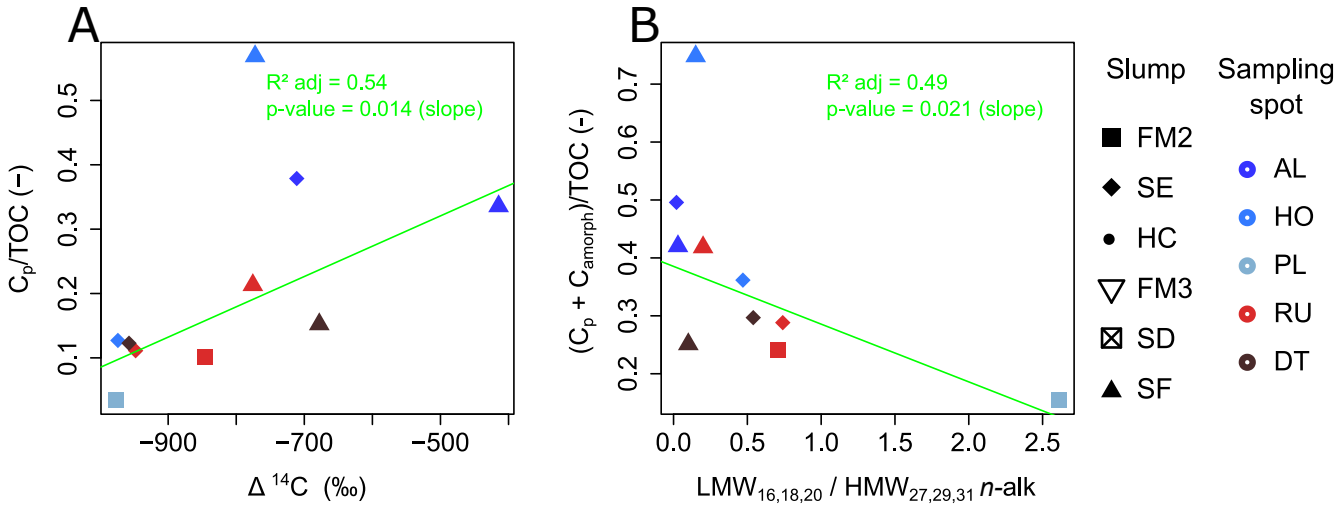

Fig. 10. Robust linear regressions for (A) Proportion of metal-OC complexes relative to TOC as a function of radiocarbon age ($\Delta^{14}C$) and (B) Sum of proportions of metals-OC complexes and maximum proportion of OC-bound to poorly crystalline Fe oxides relative to TOC as a function of high ratios of even low molecular weight n-alkanes ($LMW_{16,18,20}$) to odd high molecular weight n-alkanes ($HMW_{27,29,31}$). Low values of $LMW_{16,18,20}/HMW_{27,29,31}$ are indicative of petrogenic or microbially altered organic matter. Radiocarbon ($\Delta^{14}C$), $LMW_{16,18,20}$ and $HMW_{27,29,31}$ data from Bröder et al. (2021). Color code as in Fig. 2.

proportion of mineral-associated OC reported in Arctic soils (~30–80 %; Mueller et al 2015; Dutta et al 2006) and more generally in various soil ecosystems (23 – 96 %; Kleber et al., 2015 and references therein).

4. Conclusions

We studied seven thaw slump disturbances from the Peel Plateau, western Canadian Arctic, spanning a range of headwall heights from 2 to 25 m and an active scar zone area from 5,000 to 300,000 m^2 at the time of sampling. We compared the total and water extractable mineral element concentrations, mineralogy, and mineral-organic carbon interactions as complexes or involving (poorly) crystalline iron oxides phases between the headwall soil and sediment layers of thaw slumps and the sediments transported downstream from these disturbances. The following main conclusions can be drawn:

(i) The main mechanism of OC stabilization through mineral-organic carbon interactions within the headwall is the complexation with metals (mainly iron), which stabilizes on average 30 ± 15 % of the TOC pool with higher concentrations in near-surface layers compared to deep permafrost. In addition, up to 12 ± 5 % of the TOC is estimated to be bound to poorly crystalline iron oxides.
(ii) In the material displaced by the thaw slumps, up to 32 ± 6 % of the TOC is stabilized by organo-mineral interactions. This includes 18 ± 5 % of the TOC forming complexes with metals and up to 14 ± 4 % of the TOC bound to poorly crystalline iron oxides.
(iii) For two mega-slumps with contrasting headwall heights (slumps FM2 and FM3), modeled concentrations of organic carbon complexed with metals in the exported debris at the time of slump occurrence compared with the concentrations measured in the present displaced sediments suggests the preservation of organo-mineral complexes over recent years to decades, and likely for centuries to come.
(iv) In very large slump features, the exposure of Pleistocene-aged ice-rich tills at depth, even though less concentrated in organic carbon than permafrost above the thaw unconformity and in the active layer, induces a mass of exported TOC that exceeds the mass of TOC exported by the active layer and shallow permafrost. This is exacerbated in the largest slumps such as FM2, relative to smaller mega-slumps such as FM3 and is a consequence of the non-linearity between the thaw slump area and the volume and depth of permafrost thawed.

Demonstrating that the proportions of mineral associated OC in the material mobilized from thaw slumps remain comparable to the proportions of mineral associated OC in the headwall-origin materials supports the preservation of the organo-mineral interactions over years to centuries. Even with the known variability in mineral-organic carbon interactions within slump stratigraphic units, this supports the preservation of a portion of organic carbon that is less available for decomposition following the occurrence of a thaw slump, and therefore a pool of organic carbon that is less likely to contribute to the permafrost carbon feedback.

Declaration of Competing Interest

The authors declare that they have no known competing financial interests or personal relationships that could have appeared to influence the work reported in this paper.

Data availability

All data used in this article are available in Supporting Information S1-S6.

Acknowledgments

Research was conducted under Northwest Territories Scientific Research License 15887 within the Gwich'in Settlement Region. The authors acknowledge fieldwork support from Rosemin Nathoo, Erin MacDonald, Christine Firth, Dempster Colin, Abraham Snowshoe, Keith Colin and Andrew Koe. The authors further acknowledge Laurence Monin, Claudine Givron, Élodie Devos, and Hélène Dailly from the Mineral and Organic Chemical Analysis (MOCA) platform at UCLouvain for conducting chemical analysis, Benoît Pereira and Aubry Vandeuren for their expertise on portable X-Ray Fluorescence measurements, and the members of the WeThaw project for useful discussions. MT thanks the members of the ELIE-SOIL lab for useful critical comments. We finally acknowledge the associate editor Alberto Agnelli and two anonymous reviewers for their constructive comments.

Author contributions

MT and SO conceived and planned the experimental work. LB and KK led sampling campaign A under the supervision of JV. SZ led sampling campaign B under the supervision of ST and SK. MT realized the total concentration measurements by pXRF, and bulk elements concentration corrections for trueness with the help of AM. MT realized the selective extractions and mineralogical analysis with the help of SO. LB carried out total organic carbon concentrations measurements. MT performed the data processing. JvdS and SK provided the exported volume data of slumps FM2 and FM3 and expertise in geomorphic processes within the Peel Plateau. LB, SZ, JV, ST, SS, KK and SK contributed with their expertise on the study area. CH and AM contributed with their expertise on Fe in Arctic regions. MT wrote the manuscript under supervision of SO with inputs from all co-authors.

Funding

This project received funding from the European Union's Horizon 2020 research and innovation program under grant agreement No.714617 to SO (WeThaw), and SO acknowledges funding from the Fund for Scientific Research FNRS in Belgium (FC69480). Further funding for this work came from European Union's Horizon 2020 research and innovation program under grant agreement No.676982 to JV (Thawsome) for sampling campaign A. General support for the overall field campaign and for campaign B was provided from the Natural Sciences and Engineering Research Council of Canada (NSERC; grants nos. 430696 and 444873), the Polar Continental Shelf Program (grant 617-17) and the Campus Alberta Innovates Program. Campaign B received further support from the University of Alberta Northern Research Award to SZ.

Appendix A. Supplementary data

Supplementary data to this article can be found online at https://doi.org/10.1016/j.geoderma.2023.116443.

References

Abbott, B.W., Jones, J.B., 2015. Permafrost collapse alters soil carbon stocks, respiration, CH4, and N2O in upland tundra. Global Change Biology 21, 4570–4587. https://doi.org/10.1111/gcb.13069.

Amap, 2021. Arctic Climate Change Update 2021: Key Trends and Impacts. Summary for Policy-makers, Arctic Monitoring and Assessment Programme (AMAP), Tromsø, Norway.

Bascomb, C.L., 1968. Distribution of Pyrophosphate-Extractable Iron and Organic Carbon in Soils of Various Groups. Journal of Soil Science 19, 251–268. https://doi.org/10.1111/j.1365-2389.1968.tb01538.x.

Blakemore, L.C., Searle, P.L., Daly, B.K., 1981. Methods for chemical analysis of soils. New Zealand Soil Bur. Scientific Rep., second revision 10A. doi: 10.7931/DL1-SBSR-10A.

Bröder, L., Hirst, C., Opfergelt, S., Thomas, M., Vonk, J.E., Haghipour, N., Eglinton, T.I., Fouché, J., 2022. Contrasting Export of Particulate Organic Carbon From

Greenlandic Glacial and Nonglacial Streams. Geophysical Research Letters 49, e2022GL101210. doi: 10.1029/2022GL101210.
Bröder, L., Keskitalo, K., Zolkos, S., Shakil, S., Tank, S.E., Kokelj, S.V., Tesi, T., Van Dongen, B.E., Haghipour, N., Eglinton, T.I., Vonk, J.E., 2021. Preferential export of permafrost-derived organic matter as retrogressive thaw slumping intensifies. Environ. Res. Lett. 16 (5), 054059.
Brooker, A., Fraser, R.H., Olthof, I., Kokelj, S.V., Lacelle, D., 2014. Mapping the Activity and Evolution of Retrogressive Thaw Slumps by Tasselled Cap Trend Analysis of a Landsat Satellite Image Stack. Permafrost and Periglacial Processes 25, 243–256. https://doi.org/10.1002/ppp.1819.
Burn, C.R., 1997. Cryostratigraphy, paleogeography, and climate change during the early Holocene warm interval, western Arctic coast. Canada. Can. J. Earth Sci. 34, 912–925. https://doi.org/10.1139/e17-076.
Environment Canada, 2021. Past weather and climate. Daily/Hourly Data Report. [WWW Document]. URL https://climat.meteo.gc.ca/historical_data/search_historic_data_f.html (accessed 1.31.22).
Dalton, A.S., Margold, M., Stokes, C.R., Tarasov, L., Dyke, A.S., Adams, R.S., Allard, S., Arends, H.E., Atkinson, N., Attig, J.W., Barnett, P.J., Barnett, R.L., Batterson, M., Bernatchez, P., Borns, H.W., Breckenridge, A., Briner, J.P., Brouard, E., Campbell, J. E., Carlson, A.E., Clague, J.J., Curry, B.B., Daigneault, R.-A., Dubé-Loubert, H., Easterbrook, D.J., Franzi, D.A., Friedrich, H.G., Funder, S., Gauthier, M.S., Gowan, A.S., Harris, K.L., Hétu, B., Hooyer, T.S., Jennings, C.E., Johnson, M.D., Kehew, A.E., Kelley, S.E., Kerr, D., King, E.L., Kjeldsen, K.K., Knaeble, A.R., Lajeunesse, P., Lakeman, T.R., Lamothe, M., Larson, P., Lavoie, M., Loope, H.M., Lowell, T.V., Lusardi, B.A., Manz, L., McMartin, I., Nixon, F.C., Occhietti, S., Parkhill, M.A., Piper, D.J.W., Pronk, A.G., Richard, P.J.H., Ridge, J.C., Ross, M., Roy, M., Seaman, A., Shaw, J., Stea, R.R., Teller, J.T., Thompson, W.B., Thorleifson, L.H., Utting, D.J., Veillette, J.J., Ward, B.C., Weddle, T.K., Wright, H.E., 2020. An updated radiocarbon-based ice margin chronology for the last deglaciation of the North American Ice Sheet Complex. Quaternary Science Reviews 234, 106223.
Daly, B.K., 1982. Identification of podzols and podzolised soils in New Zealand by relative absorbance of oxalate extracts of A and B horizons. Geoderma 28, 29–38. https://doi.org/10.1016/0016-7061(82)90038-6.
Dobricic, S., Pozzoli, L., 2019. Arctic permafrost thawing: impacts on high latitude emissions of carbon dioxide and methane. Publications Office of the European Union, LU.
Duk-Rodkin, A., Hughes, O.L., 1992. Surficial Geology, Fort McPherson-Bell River. Yukon-Northwest Territories, Geological Survey of Canada.
Dutta, K., Schuur, E. a. G., Neff, J.C., Zimov, S.A., 2006. Potential carbon release from permafrost soils of Northeastern Siberia. Global Change Biology 12, 2336–2351. doi: 10.1111/j.1365-2486.2006.01259.x.
Fox-Kemper, B., Hewitt, H.T., Xiao, C., Aðalgeirsdóttir, G., Drijfhout, S.S., Edwards, T.L., Golledge, N.R., Hemer, M., Koop, R.E., Krinner, G., Mix, A., Notz, D., Nowicki, S., Nurhati, I.S., Ruiz, L., Sallée, J.-B., Slangen, A.B.A., Yu, Y., 2021. Ocean, Cryosphere and Sea Level Change, in: Masson-Delmotte, V., Zhai, P., Pirani, A., Connors, S.L., Péan, C., Berger, S., Caud, N., Chen, Y., Goldfarb, L., Gomis, M.I., Huang, M., Leitzell, K., Lonnoy, E., Matthews, J.B.R., Maycock, T.K., Waterfield, T., Yelekçi, O., Yu, R., Zhou, B. (Eds.), Climate Change 2021: The Physical Science Basis. Contribution of Working Group I to the Sixth Assessment Report of the Intergovernmental Panel on Climate Change. Cambridge University Press, Cambridge, United Kingdom and New York, NY, USA, pp. 1211–1362.
Friedlingstein, P., Cox, P., Betts, R., Bopp, L., von Bloh, W., Brovkin, V., Cadule, P., Doney, S., Eby, M., Fung, I., Bala, G., John, J., Jones, C., Joos, F., Kato, T., Kawamiya, M., Knorr, W., Lindsay, K., Matthews, H.D., Raddatz, T., Rayner, P., Reick, C., Roeckner, E., Schnitzler, K.-G., Schnur, R., Strassmann, K., Weaver, A.J., Yoshikawa, C., Zeng, N., 2006. Climate-Carbon Cycle Feedback Analysis: Results from the C4MIP Model Intercomparison. J. Climate 19, 3337–3353. https://doi.org/10.1175/JCLI3800.1.
Heginbottom, J.A., Brown, J., Humlum, O., Svensson, H., 2012. Permafrost and Periglacial Environments, in: State of the Earth's Cryosphere at the Beginning of the 21st Century : Glaciers, Global Snow Cover, Floating Ice, and Permafrost and Periglacial Environments, USGS 1386 Series Professional Paper. U.S. Geological Survey, Reston, VA, pp. A425–A496.
Herndon, E., Kinsman-Costello, L., Godsey, S., 2020. Biogeochemical Cycling of Redox-Sensitive Elements in Permafrost-Affected Ecosystems. Biogeochemical Cycles. American Geophysical Union (AGU) 245–265.
Hintze, J.L., Nelson, R.D., 1998. Violin Plots: A Box Plot-Density Trace Synergism. The American Statistician 52, 181. https://doi.org/10.2307/2685478.
Hugelius, G., Strauss, J., Zubrzycki, S., Harden, J.W., Schuur, E.A.G., Ping, C.-L., Schirrmeister, L., Grosse, G., Michaelson, G.J., Koven, C.D., O'Donnell, J.A., Elberling, B., Mishra, U., Camill, P., Yu, Z., Palmtag, J., Kuhry, P., 2014. Estimated stocks of circumpolar permafrost carbon with quantified uncertainty ranges and identified data gaps. Biogeosciences 11 (23), 6573–6593.
IPCC, 2019. IPCC Special Report on the Ocean and Cryosphere in a Changing Climate: Summary for Policymakers., in: Pörtner, H.-O., Roberts, D.C., Masson-Delmotte, V., Zhai, P., Tignor, M., Poloczanska, E., Mintenbeck, K., Nicolai, M., Okem, A., Petzold, J., Rama, B., Weyer, N. (Eds.), .
Iwahana, G.o., Machimura, T., Kobayashi, Y., Fedorov, A.N., Konstantinov, P.Y., Fukuda, M., 2005. Influence of forest clear-cutting on the thermal and hydrological regime of the active layer near Yakutsk, eastern Siberia. Journal of Geophysical Research: Biogeosciences 110 (G2), n/a–n/a.
Jeanroy, E., Guillet, B., 1981. The occurrence of suspended ferruginous particles in pyrophosphate extracts of some soil horizons. Geoderma 26, 95–105. https://doi.org/10.1016/0016-7061(81)90078-1.
Kaiser, K., Guggenberger, G., 2007. Sorptive stabilization of organic matter by microporous goethite: sorption into small pores vs. surface complexation. European Journal of Soil Science 58, 45–59. https://doi.org/10.1111/j.1365-2389.2006.00799.x.
Keskitalo, K.H., Bröder, L., Shakil, S., Zolkos, S., Tank, S.E., van Dongen, B.E., Tesi, T., Haghipour, N., Eglinton, T.I., Kokelj, S.V., Vonk, J.E., 2021. Downstream Evolution of Particulate Organic Matter Composition From Permafrost Thaw Slumps. Front. Earth Sci. 9 https://doi.org/10.3389/feart.2021.642675.
Kleber, M., Eusterhues, K., Keiluweit, M., Mikutta, C., Mikutta, R., Nico, P.S., 2015. Chapter One - Mineral-Organic Associations: Formation, Properties, and Relevance in Soil Environments. In: Sparks, D.L. (Ed.), Advances in Agronomy. Academic Press, pp. 1–140. https://doi.org/10.1016/bs.agron.2014.10.005.
Knoblauch, C., Beer, C., Schuett, A., Sauerland, L., Liebner, S., Steinhof, A., Rethemeyer, J., Grigoriev, M.N., Faguet, A., Pfeiffer, E.-M., 2021. Carbon Dioxide and Methane Release Following Abrupt Thaw of Pleistocene Permafrost Deposits in Arctic Siberia. Journal of Geophysical Research: Biogeosciences 126, e2021JG006543. doi: 10.1029/2021JG006543.
Kögel-Knabner, I., Guggenberger, G., Kleber, M., Kandeler, E., Kalbitz, K., Scheu, S., Eusterhues, K., Leinweber, P., 2008. Organo-mineral associations in temperate soils: Integrating biology, mineralogy, and organic matter chemistry. Journal of Plant Nutrition and Soil Science 171, 61–82. https://doi.org/10.1002/jpln.200700048.
Kokelj, S.V., Burn, C.R., 2005. Geochemistry of the active layer and near-surface permafrost, Mackenzie delta region, Northwest Territories. Canada. Can. J. Earth Sci. 42, 37–48. https://doi.org/10.1139/e04-089.
Kokelj, S.V., Tunnicliffe, J., Lacelle, D., Lantz, T., Fraser, R., 2015a. Retrogressive thaw slumps: From slope process to the landscape sensitivity of northwestern Canada. Presented at the GeoQuebec 2015 Conference, Quebec City, Quebec, Canada.
Kokelj, S.V., Jorgenson, M.T., 2013. Advances in Thermokarst Research. Permafrost and Periglacial Processes 24, 108–119. https://doi.org/10.1002/ppp.1779.
Kokelj, S.V., Lantz, T.C., Kanigan, J., Smith, S.L., Coutts, R., 2009. Origin and polycyclic behaviour of tundra thaw slumps, Mackenzie Delta region, Northwest Territories, Canada. Permafrost and Periglacial Processes 20, 173–184. https://doi.org/10.1002/ppp.642.
Kokelj, S.V., Tunnicliffe, J., Lacelle, D., Lantz, T.C., Chin, K.S., Fraser, R., 2015b. Increased precipitation drives mega slump development and destabilization of ice-rich permafrost terrain, northwestern Canada. Global and Planetary Change 129, 56–68. https://doi.org/10.1016/j.gloplacha.2015.02.008.
Kokelj, S.V., Lantz, T.C., Tunnicliffe, J., Segal, R., Lacelle, D., 2017a. Climate-driven thaw of permafrost preserved glacial landscapes, northwestern Canada. Geology 45, 371–374. https://doi.org/10.1130/G38626.1.
Kokelj, S.V., Tunnicliffe, J.F., Lacelle, D., 2017b. The Peel Plateau of Northwestern Canada: An Ice-Rich Hummocky Moraine Landscape in Transition. In: Slaymaker, O. (Ed.), Landscapes and Landforms of Western Canada, World Geomorphological Landscapes. Springer International Publishing, Cham, pp. 109–122. https://doi.org/10.1007/978-3-319-44595-3_7.
Kokelj, S.V., Kokoszka, J., van der Sluijs, J., Rudy, A.C.A., Tunnicliffe, J., Shakil, S., Tank, S.E., Zolkos, S., 2021. Thaw-driven mass wasting couples slopes with downstream systems, and effects propagate through Arctic drainage networks. The Cryosphere 15, 3059–3081. https://doi.org/10.5194/tc-15-3059-2021.
Koven, C.D., Ringeval, B., Friedlingstein, P., Ciais, P., Cadule, P., Khvorostyanov, D., Krinner, G., Tarnocai, C., 2011. Permafrost carbon-climate feedbacks accelerate global warming. PNAS 108, 14769–14774. https://doi.org/10.1073/pnas.1103910108.
Lacelle, D., Bjornson, J., Lauriol, B., 2010. Climatic and geomorphic factors affecting contemporary (1950–2004) activity of retrogressive thaw slumps on the Aklavik Plateau, Richardson Mountains, NWT, Canada. Permafrost and Periglacial Processes 21, 1–15. https://doi.org/10.1002/ppp.666.
Lacelle, D., Brooker, A., Fraser, R.H., Kokelj, S.V., 2015a. Distribution and growth of thaw slumps in the Richardson Mountains-Peel Plateau region, northwestern Canada. Geomorphology 235, 40–51. https://doi.org/10.1016/j.geomorph.2015.01.024.
Lacelle, D., Fontaine, M., Kokelj, S., 2015b. Geochemistry of the active layer and permafrost in northwestern Canada: from measurements to Quaternary stratigraphy.
Lacelle, D., Lauriol, B., Zazula, G., Ghaleb, B., Utting, N., Clark, I.D., 2013. Timing of advance and basal condition of the Laurentide Ice Sheet during the last glacial maximum in the Richardson Mountains, NWT. Quaternary Research 80, 274–283. https://doi.org/10.1016/j.yqres.2013.06.001.
Lacelle, D., Fontaine, M., Pellerin, A., Kokelj, S.V., Clark, I.D., 2019. Legacy of Holocene Landscape Changes on Soil Biogeochemistry: A Perspective From Paleo-Active Layers in Northwestern Canada. Journal of Geophysical Research: Biogeosciences 124, 2662–2679. https://doi.org/10.1029/2018JG004916.
Lalonde, K., Mucci, A., Ouellet, A., Gélinas, Y., 2012. Preservation of organic matter in sediments promoted by iron. Nature 483, 198–200. https://doi.org/10.1038/nature10855.
Lantuit, H., Pollard, W.H., Couture, N., Fritz, M., Schirrmeister, L., Meyer, H., Hubberten, H.-W., 2012. Modern and Late Holocene Retrogressive Thaw Slump Activity on the Yukon Coastal Plain and Herschel Island, Yukon Territory, Canada. Permafrost and Periglacial Processes 23, 39–51. https://doi.org/10.1002/ppp.1731.
Lawrence, D.M., Koven, C.D., Swenson, S.C., Riley, W.J., Slater, A.G., 2015. Permafrost thaw and resulting soil moisture changes regulate projected high-latitude CO 2 and CH 4 emissions. Environ. Res. Lett. 10 (9), 094011.
Lewkowicz, A.G., Way, R.G., 2019. Extremes of summer climate trigger thousands of thermokarst landslides in a High Arctic environment. Nature Communications 10, 1329. https://doi.org/10.1038/s41467-019-09314-7.
Littlefair, C.A., Tank, S.E., 2018. Biodegradability of Thermokarst Carbon in a Till-Associated, Glacial Margin Landscape: The Case of the Peel Plateau, NWT, Canada. Journal of Geophysical Research: Biogeosciences 123, 3293–3307. https://doi.org/10.1029/2018JG004461.

Littlefair, C.A., Tank, S.E., Kokelj, S.V., 2017. Retrogressive thaw slumps temper dissolved organic carbon delivery to streams of the Peel Plateau, NWT, Canada. Biogeosciences 14, 5487–5505. https://doi.org/10.5194/bg-14-5487-2017.

Lützow, M.v., Kögel-Knabner, I., Ekschmitt, K., Matzner, E., Guggenberger, G., Marschner, B., Flessa, H., 2006. Stabilization of organic matter in temperate soils: mechanisms and their relevance under different soil conditions – a review. European Journal of Soil Science 57 (4), 426–445.

Malone, L., Lacelle, D., Kokelj, S., Clark, I.D., 2013. Impacts of hillslope thaw slumps on the geochemistry of permafrost catchments (Stony Creek watershed, NWT, Canada). Chemical Geology 356, 38–49. https://doi.org/10.1016/j.chemgeo.2013.07.010.

McGill, R., Tukey, J.W., Larsen, W.A., 1978. Variations of Box Plots. The American Statistician 32, 12–16. https://doi.org/10.2307/2683468.

McGuire, A.D., Lawrence, D.M., Koven, C., Clein, J.S., Burke, E., Chen, G., Jafarov, E., MacDougall, A.H., Marchenko, S., Nicolsky, D., Peng, S., Rinke, A., Ciais, P., Gouttevin, I., Hayes, D.J., Ji, D., Krinner, G., Moore, J.C., Romanovsky, V., Schädel, C., Schaefer, K., Schuur, E.A.G., Zhuang, Q., 2018. Dependence of the evolution of carbon dynamics in the northern permafrost region on the trajectory of climate change. PNAS 115, 3882–3887. https://doi.org/10.1073/pnas.1719903115.

McKeague, J.A., Day, J.H., 1966. Dithionite- and Oxalate-Extractable Fe and Al as Aids in Differentiating Various Classes of Soils. Can. J. Soil. Sci. 46, 13–22. https://doi.org/10.4141/cjss66-003.

Mehra, O.P., Jackson, M.L., 1958. Iron Oxide Removal from Soils and Clays by a Dithionite-Citrate System Buffered with Sodium Bicarbonate. Clays Clay Miner. 7, 317–327. https://doi.org/10.1346/CCMN.1958.0070122.

Meredith, M., Sommerkorn, M., Cassotta, S., Derksen, C., Ekaykin, A., Hollowed, A., Kofinas, G., Mackintosh, A., Melbourne-Thomas, J., Muelbert, M.M.C., Ottersen, G., Pritchard, H., Schuur, E.A.G., 2019. Polar Regions. In: Pörtner, H.-.-O., Roberts, D.C., Masson-Delmotte, V., Zhai, P., Tignor, M., Poloczanska, E., Mintenbeck, K., Alegría, A., Nicolai, M., Okem, A., Petzold, J., Rama, B., Weyer, N.M. (Eds.), IPCC Special Report on the Ocean and Cryosphere in a Changing Climate. Cambridge University Press, Cambridge, UK and New York, NY, USA, pp. 203–320.

Monhonval, A., Mauclet, E., Pereira, B., Vandeuren, A., Strauss, J., Grosse, G., Schirrmeister, L., Fuchs, M., Kuhry, P., Opfergelt, S., 2021a. Mineral Element Stocks in the Yedoma Domain: A Novel Method Applied to Ice-Rich Permafrost Regions. Frontiers in Earth Science 9, 773. https://doi.org/10.3389/feart.2021.703304.

Monhonval, A., Strauss, J., Mauclet, E., Hirst, C., Bemelmans, N., Grosse, G., Schirrmeister, L., Fuchs, M., Opfergelt, S., 2021b. Iron Redistribution Upon Thermokarst Processes in the Yedoma Domain. Front. Earth Sci. https://doi.org/10.3389/feart.2021.703339.

Monhonval, A., Strauss, J., Thomas, M., Hirst, C., Titeux, H., Louis, J., Gilliot, A., du Bois d'Aische, E., Pereira, B., Vandeuren, A., Grosse, G., Schirrmeister, L., Jongejans, L.L., Ulrich, M., Opfergelt, S., 2022. Thermokarst processes increase the supply of stabilizing surfaces and elements (Fe, Mn, Al, and Ca) for mineral–organic carbon interactions. Permafrost and Periglacial Processes 33, 452–469. https://doi.org/10.1002/ppp.2162.

Mu, C.C., Zhang, T.J., Zhao, Q., Guo, H., Zhong, W., Su, H., Wu, Q.B., 2016. Soil organic carbon stabilization by iron in permafrost regions of the Qinghai-Tibet Plateau. Geophysical Research Letters 43, 10286–10294. https://doi.org/10.1002/2016GL070071.

Mu, C., Zhang, F., Mu, M., Chen, X., Li, Z., Zhang, T., 2020. Organic carbon stabilized by iron during slump deformation on the Qinghai-Tibetan Plateau. CATENA 187, 104282. https://doi.org/10.1016/j.catena.2019.104282.

Mueller, C.W., Rethemeyer, J., Kao-Kniffin, J., Löppmann, S., Hinkel, K.M., Bockheim, G., J.,, 2015. Large amounts of labile organic carbon in permafrost soils of northern Alaska. Global Change Biology 21, 2804–2817. https://doi.org/10.1111/gcb.12876.

Murton, J.B., Ballantyne, C.K., 2017. Chapter 5 Periglacial and permafrost ground models for Great Britain. Geol. Soc. London Eng. Geol. Spec. Publ. 28, 501–597. doi: 10.1144/EGSP28.5.

O'Neill, H.B., Burn, C.R., Kokelj, S.V., Lantz, T.C., 2015. 'Warm' Tundra: Atmospheric and Near-Surface Ground Temperature Inversions Across an Alpine Treeline in Continuous Permafrost, Western Arctic, Canada. Permafrost and Periglacial Processes 26, 103–118. https://doi.org/10.1002/ppp.1838.

Obu, J., Westermann, S., Kääb, A., Bartsch, A., 2018. Ground Temperature Map, 2000-2016, Northern Hemisphere Permafrost. Alfred Wegener Institute, Helmholtz Centre for Polar and Marine Research, Bremerhaven. doi: 10.1594/PANGAEA.888600.

Opfergelt, S., 2020. The next generation of climate model should account for the evolution of mineral-organic interactions with permafrost thaw. Environ. Res. Lett. 15 (9), 091003.

Parfitt, R.L., Childs, C.W., 1988. Estimation of forms of Fe and Al - a review, and analysis of contrasting soils by dissolution and Mossbauer methods. Soil Res. 26, 121–144. https://doi.org/10.1071/sr9880121.

Patzner, M.S., Mueller, C.W., Malusova, M., Baur, M., Nikeleit, V., Scholten, T., Hoeschen, C., Byrne, J.M., Borch, T., Kappler, A., Bryce, C., 2020. Iron mineral dissolution releases iron and associated organic carbon during permafrost thaw. Nat Commun 11, 6329. https://doi.org/10.1038/s41467-020-20102-6.

Plaza, C., Pegoraro, E., Bracho, R., Celis, G., Crummer, K.G., Hutchings, J.A., Hicks Pries, C.E., Mauritz, M., Natali, S.M., Salmon, V.G., Schädel, C., Webb, E.E., Schuur, E.A.G., 2019. Direct observation of permafrost degradation and rapid soil carbon loss in tundra. Nat. Geosci. 12, 627–631. https://doi.org/10.1038/s41561-019-0387-6.

R Core Team, 2019. R: A Language and Environment for Statistical Computing. Austria, Vienna.

Ravansari, R., Wilson, S.C., Tighe, M., 2020. Portable X-ray fluorescence for environmental assessment of soils: Not just a point and shoot method. Environment International 134, 105250. https://doi.org/10.1016/j.envint.2019.105250.

Reimann, C., Filzmoser, P., Garrett, R., Dutter, R., 2008. Statistical Data Analysis Explained: Applied Environmental Statistics with R, in: Statistical Data Analysis Explained: Applied Environmental Statistics with R.

Rennert, T., 2019. Wet-chemical extractions to characterise pedogenic Al and Fe species – a critical review. Soil Res. 57, 1–16. https://doi.org/10.1071/SR18299.

Schädel, C., Bader, M.-K.-F., Schuur, E.A.G., Biasi, C., Bracho, R., Čapek, P., De Baets, S., Diáková, K., Ernakovich, J., Estop-Aragones, C., Graham, D.E., Hartley, I.P., Iversen, C.M., Kane, E., Knoblauch, C., Lupascu, M., Martikainen, P.J., Natali, S.M., Norby, R.J., O'Donnell, J.A., Chowdhury, T.R., Šantrůčková, H., Shaver, G., Sloan, V. L., Treat, C.C., Turetsky, M.R., Waldrop, M.P., Wickland, K.P., 2016. Potential carbon emissions dominated by carbon dioxide from thawed permafrost soils. Nature Clim Change 6, 950–953. https://doi.org/10.1038/nclimate3054.

Schuur, E., Bockheim, J., Canadell, J.G., Euskirchen, E., Field, C., Goryachkin, S., Hagemann, S., Kuhry, P., Lafleur, P.M., Lee, H., Mazhitova, G., Nelson, F.E., Rinke, A., Romanovsky, V.E., Shiklomanov, N., Tarnocai, C., Venevsky, S., Vogel, J. G., Zimov, S.A., 2008. Vulnerability of Permafrost Carbon to Climate Change: Implications for the Global Carbon Cycle. BioScience 58, 701–714. https://doi.org/10.1641/B580807.

Schuur, E.A.G., McGuire, A.D., Schädel, C., Grosse, G., Harden, J.W., Hayes, D.J., Hugelius, G., Koven, C.D., Kuhry, P., Lawrence, D.M., Natali, S.M., Olefeldt, D., Romanovsky, V.E., Schaefer, K., Turetsky, M.R., Treat, C.C., Vonk, J.E., 2015. Climate change and the permafrost carbon feedback. Nature 520 (7546), 171–179.

Shakil, S., Tank, S.E., Kokelj, S.V., Vonk, J.E., Zolkos, S., 2020. Particulate dominance of organic carbon mobilization from thaw slumps on the Peel Plateau, NT: Quantification and implications for stream systems and permafrost carbon release. Environ. Res. Lett. 15 (11), 114019.

Shakil, S., Tank, S.E., Vonk, J.E., Zolkos, S., 2022. Low biodegradability of particulate organic carbon mobilized from thaw slumps on the Peel Plateau, NT, and possible chemosynthesis and sorption effects. Biogeosciences 19, 1871–1890. https://doi.org/10.5194/bg-19-1871-2022.

Strauss, J., Schirrmeister, L., Grosse, G., Fortier, D., Hugelius, G., Knoblauch, C., Romanovsky, V., Schädel, C., Schneider von Deimling, T., Schuur, E.A.G., Shmelev, D., Ulrich, M., Veremeeva, A., 2017. Deep Yedoma permafrost: A synthesis of depositional characteristics and carbon vulnerability. Earth-Science Reviews 172, 75–86. https://doi.org/10.1016/j.earscirev.2017.07.007.

Tanski, G., Bröder, L., Wagner, D., Knoblauch, C., Lantuit, H., Beer, C., Sachs, T., Fritz, M., Tesi, T., Koch, B.P., Haghipour, N., Eglinton, T.I., Strauss, J., Vonk, J.E., 2021. Permafrost Carbon and CO2 Pathways Differ at Contrasting Coastal Erosion Sites in the Canadian Arctic. Frontiers in Earth Science 9.

Tanski, G., Lantuit, H., Ruttor, S., Knoblauch, C., Radosavljevic, B., Strauss, J., Wolter, J., Irrgang, A.M., Ramage, J., Fritz, M., 2017. Transformation of terrestrial organic matter along thermokarst-affected permafrost coasts in the Arctic. Sci. Total Environ. 581–582, 434–447. https://doi.org/10.1016/j.scitotenv.2016.12.152.

Turetsky, M.R., Abbott, B.W., Jones, M.C., Anthony, K.W., Olefeldt, D., Schuur, E.A.G., Grosse, G., Kuhry, P., Hugelius, G., Koven, C., Lawrence, D.M., Gibson, C., Sannel, A. B.K., McGuire, A.D., 2020. Carbon release through abrupt permafrost thaw. Nature Geoscience 13, 138–143. https://doi.org/10.1038/s41561-019-0526-0.

Van der Sluijs, J., Kokelj, S.V., Fraser, R.H., Tunnicliffe, J., Lacelle, D., 2018. Permafrost Terrain Dynamics and Infrastructure Impacts Revealed by UAV Photogrammetry and Thermal Imaging. Remote Sensing 10, 1734. https://doi.org/10.3390/rs10111734.

van der Sluijs, J., Kokelj, S.V., Tunnicliffe, J.F., 2022. Allometric scaling of retrogressive thaw slumps. The Cryosphere Discussions 1–30. https://doi.org/10.5194/tc-2022-149.

Vonk, J.E., Mann, P.J., Davydov, S., Davydova, A., Spencer, R.G.M., Schade, J., Sobczak, W.V., Zimov, N., Zimov, S., Bulygina, E., Eglinton, T.I., Holmes, R.M., 2013. High biolability of ancient permafrost carbon upon thaw. Geophys. Res. Lett. 40, 2689–2693. https://doi.org/10.1002/grl.50348.

Wagai, R., Mayer, L.M., 2007. Sorptive stabilization of organic matter in soils by hydrous iron oxides. Geochimica et Cosmochimica Acta 71, 25–35. https://doi.org/10.1016/j.gca.2006.08.047.

Young, J.M., Alvarez, A., van der Sluijs, J., Kokelj, S.V., Rudy, A., McPhee, A., Stoker, B. J., Margold, M., Froese, D., 2022. Recent Intensification (2004–2020) of Permafrost Mass-Wasting in the Central Mackenzie Valley Foothills Is a Legacy of Past Forest Fire Disturbances. Geophysical Research Letters 49 (24).

Zimov, S.A., Schuur, E.A.G., Chapin, F.S., 2006. Permafrost and the Global Carbon Budget. Science 312 (5780), 1612–1613.

Zolkos, S., Tank, S.E., 2019. Permafrost geochemistry and retrogressive thaw slump morphology (Peel Plateau, Canada) v. 1.0 (2017-2017). doi: 10.5885/45573XD-28DD57D553F14BF0.

Zolkos, S., Tank, S., 2020. Experimental evidence for the roles of permafrost thaw history and mineral composition within inorganic carbon cycling in thermokarst-affected stream networks. Front. Earth Sci. 8 https://doi.org/10.3389/feart.2020.00152.

Zolkos, S., Tank, S.E., Kokelj, S.V., 2018. Mineral Weathering and the Permafrost Carbon-Climate Feedback. Geophysical Research Letters 45, 9623–9632. https://doi.org/10.1029/2018GL078748.